Liquid water path variability in unbroken marine stratocumulus cloud

ROBERT WOOD[1] and JONATHAN P. TAYLOR

The Met Office, Farnborough, UK

4 December 2000

SUMMARY

Liquid water path variability in unbroken marine stratocumulus clouds is examined using a simple adiabatic model and both ground based and airborne observations. Observations from FIRE suggest that fluctuations in liquid water path at scales smaller than around 60 km can be modelled reasonably well as a function of fluctuations in cloud-base height. A simple adiabatic model of cloud liquid water content with a normally distributed cloud-base and constant inversion height results in liquid water path distributions that compare favourably with observations. Further, it is shown how cloud-base height fluctuations can be predicted from the subcloud turbulent fluctuations of temperature, specific humidity and their covariance. The relative importance of these three contributing terms is assessed. Aircraft observations of these fluctuating variables are used to predict the widths of liquid water path distributions observed radiometrically. The observations also suggest that the standard deviation of cloud-base height and hence liquid water path variability increases with increasing boundary layer depth. The model liquid water path distributions could be used to derive plane-parallel albedo biases and offer a possible framework for future parameterisations of subgrid-scale variability in GCMs.

Keywords: Stratocumulus, Liquid water path, Spatial variability

1 Introduction

Cloud radiative properties are of prime importance in the determination of cloud-climate interactions. Calculation of the radiative properties of inhomogeneous clouds remains a central problem in cloud physics, and has been a major focus of recent interest (Cahalan et al, 1994; Hignett and Taylor, 1996; Marshak *et al.*, 1998). Stephens (1986) showed that a cloud with an inhomogeneous horizontal distribution of liquid water has a lower albedo than the cloud with a uniform liquid water content given that the clouds have the same mean liquid water content. Cahalan *et al.* (1994) showed that the in-cloud structure of stratocumulus has a greater effect upon the mesoscale mean albedo than cloud fraction because the plane-parallel albedo bias is largest when the cloud fraction reaches 100%. It is important therefore to be able to quantify the degree of inhomogeneity in continuous stratocumulus cloud sheets if accurate parameterisations are to be developed for use in large-scale numerical models. There are other reasons why inhomogeneity within stratocumulus cloud may be important. Numerical studies of autoconversion of cloud water into rain water (Berry and Reinhardt, 1974; Tripoli and Cotton, 1980; Liou and Ou, 1989; Austin et al, 1995) show a very strong increase in the autoconversion rate with increasing liquid water content. An inhomogeneous cloud containing regions of enhanced and reduced liquid water content might therefore produce substantially higher rates of drizzle precipitation than a homogeneously distributed cloud of identical mean liquid water content (e.g. Larson *et al.*, 2000; Pincus and Klein 2000; Rotstayn 2000). Indeed, studies of drizzle formation within stratiform cloud sheets show regions of enhanced precipitation occurring in coherent patches with horizontal scales considerably larger than the boundary layer depth (Austin *et al.*, 1995). These studies give further impetus to the characterisation and understanding of inhomogeneity in stratocumulus cloud.

There is a considerable body of observational evidence showing that stratocumulus cloud exhibits adiabatic or near-adiabatic profiles of liquid water content (Slingo et al, 1982; Gerber et al, 1994; Brenguier *et al.*, 2000; Pawlowska, 2000), although there are cases where stratocumulus clouds exhibit profiles

[1]Corresponding author address: Meteorological Research Flight, Y46 Building, DERA, Farnborough, Hants, GU14 0LX, UK.
Email: robwood@meto.gov.uk

of liquid water content that are somewhat sub-adiabatic (e.g. Austin *et al.*, 1995; Nicholls and Leighton, 1986). Whether the subadiabaticity is a result of instrument droplet sampling problems remains a topic for debate. The subadiabaticity is most likely a true physical effect resulting from strong entrainment or drizzle depletion of liquid water. The assumptions that the local liquid water content within cloud is adiabatic and that at a given level regions of enhanced liquid water content correspond to regions where the local cloud-base is lower are central to the model of Considine *et al.* (1997) - henceforth CCW. The probability distribution function (pdf) of liquid water path (*LWP*) in the cloud is then related to the distribution of cloud-base height and the mean cloud thickness only, assuming that cloud-top height fluctuations are small in comparison with cloud-base fluctuations. This approach presents an attractive framework within which horizontal variability can be studied.

This study exmamines the CCW model using simultaneous observations of stratocumulus liquid water path and cloud-base height from the First ICCP Regional Experiment (FIRE, Albrecht et al. 1988). The work is then extended to the prediction of cloud-base variability from boundary layer turbulent parameters for which observational evidence is presented linking the cloud-base height variability to the standard deviations of the temperature and humidity and their covariance. Section 2 gives some details of the model of CCW. Section 3 presents a possible framework for the prediction of the cloud-base variability in marine stratocumulus. Section 4 presents observational results to validate the two models. Finally, there is a discussion on the possible parameterisation of the cloud-base and *LWP* variability for use in GCMs.

2 The model of Considine *et al.* (1997)

The CCW model is used to derive a relationship between the mean *LWP* (or cloud thickness), the standard deviation of the cloud-base height and the standard deviation of *LWP*. Only three assumptions are made concerning the nature of the cloud: (1) the cloud-base height is normally distributed with standard deviation σ_{CB} around a mean value; (2) the cloud-top height does not vary; (3) the liquid water content (*LWC*) at any point in the cloud is determined entirely by the assumption of adiabaticity, i.e. the *LWC* increases linearly[2] with vertical distance from the cloud-base. Following these assumptions the *LWP* obtained by assuming an adiabatic cloud with a cloud thickness h equal to the difference between the cloud-top height and the mean cloud-base height is given by

$$LWP_{adiab} = \frac{1}{2}\Gamma_{adiab}h^2 \tag{1}$$

where $\Gamma_{adiab}$is the adiabatic rate of change of liquid water content with height. Liquid water path pdfs (see CCW) are generated using the relation

$$P(h)dh = P(LWP)d(LWP) \tag{2}$$

where $P(h)$ is the pdf of the cloud thickness and $P(LWP)$ is the pdf of *LWP*. Assuming $P(h)$ to be normally distributed (mean $\overline{h}$ and standard deviation σ_{CB}), then

$$P(h) = \frac{1}{\sigma_{CB}\sqrt{2\pi}}\exp\left\{-\frac{\left(h-\overline{h}\right)^2}{2\sigma_{CB}^2}\right\}. \tag{3}$$

Then, using (2) to change the variable from cloud thickness to *LWP*, one obtains the expression of CCW

$$P(LWP) = \frac{1}{\sigma_{CB}\sqrt{4\pi\Gamma_{adiab}LWP}}\exp\left\{-\frac{\left(h-\overline{h}\right)^2}{2\sigma_{CB}^2}\right\}. \tag{4}$$

The mean liquid water path is given by the expression

$$\overline{LWP} = \frac{1}{2}\Gamma_{adiab}\left(\overline{h}^2 + \sigma_{CB}^2\right). \tag{5}$$

The standard deviation of the liquid water path is given, to better than 5% (for $\sigma_{CB}/h < 0.5$) by

$$\frac{\sigma_{LWP}}{\sigma_{CB}} = \sqrt{2}\Gamma^{\frac{1}{2}}_{adiab}\overline{LWP}^{\frac{1}{2}}. \tag{6}$$

Combining (1) and (5) and substituting into (4) gives

[2]The gradient of the adiabatic *LWC* does change with height but through the depth of a thin cloud such as stratocumulus its change is very small.

$$P(LWP) = \frac{1}{\sigma_{CB}\sqrt{4\pi\Gamma_{adiab}LWP}}\exp\left[-\frac{\left\{LWP^{\frac{1}{2}} - \left(\overline{LWP} - \frac{1}{2}\Gamma_{adiab}\sigma_{CB}^2\right)^{\frac{1}{2}}\right\}^2}{\Gamma_{adiab}\sigma_{CB}^2}\right]. \qquad (7)$$

which defines the LWP pdf with only $\overline{LWP}$, σ_{CB} and Γ_{adiab} as input parameters.

3 Determination of cloud-base height variability

The horizontal variability of LWP is determined using (4) and is strongly dependent upon the standard deviation of the cloud-base height. It would therefore be useful to be able to determine this parameter from fluctuating boundary layer thermodynamic parameters. A constant-height reference level (height z_0) is chosen some distance below cloud-base (local height z_{CB}). If one assumes the presence of a well-mixed dry adiabatic atmosphere in any column from the reference level to the cloud-base at zenith then it is possible to use observed fluctuations in temperature and specific humidity to determine the distance from the reference level to the cloud-base. Here we make the assumption that both the specific humidity and the temperature are normally distributed at the reference level

$$q_0 = \mathbf{N}\left(\overline{q}_0, \sigma_{q_0}\right); \qquad T_0 = \mathbf{N}\left(\overline{T}_0, \sigma_{T_0}\right) \qquad (8)$$

where $\overline{q}_0$ and $\overline{T}_0$ are the means, and σ_{q_0} and σ_{T_0} the standard deviations of specific humidity and temperature respectively. It is assumed that the specific humidity and the temperature at a height z ($z_0 < z < z_{CB}$) are given by

$$q(z) = q_0; \qquad T(z) = T_0 - \Gamma_{dry}(z - z_0) \qquad (9)$$

where Γ_{dry} is the dry adiabatic lapse rate. The saturation specific humidity $q_{sat}(z)$ is a function of both temperature and pressure at z. The pressure as a function of height above the reference level is calculated using the hydrostatic equation. In this analysis the saturation specific humidity is calculated using the relationship

$$q_{sat}(T,p) = \frac{1023.3011 - 7.7069T + 0.01455T^2}{p}. \qquad (10)$$

Equation (10) is accurate to better than 5% over the temperature range [270-300K] and pressure range [750-1050 hPa]. The local cloud-base height z_{CB} is then determined by combining (9), the hydrostatic equation and (10) with the condition that

$$q_{sat}(T(z_{CB}), p(z_{CB})) = q_0 : \qquad (11)$$

$$z_{CB} - z_0 = \frac{T_0 - 264.842 - 8.289(p_0q_0 - 2.7463)^{\frac{1}{2}}}{\Gamma_{dry} - 8.289p_0q_0g/2RT_0(p_0q_0 - 2.7463)^{\frac{1}{2}}}. \qquad (12)$$

Equation (12) presents an expression for calculating the vertical distance from the reference level to the local cloud-base given the three reference-level parameters (T_0, p_0, q_0). In the derivation of (12) a further simplification of the solution to the hydrostatic equation is made that gives $z_{CB} - z_0$ to better than 4 m providing that $z_{CB} - z_0 < 200$ m. This condition will apply if the reference level is chosen to be as close to cloud-base as possible without being higher than the cloud-base at any horizontal position. If the standard deviation of the cloud-base height is greater than around 100 m then there are likely to be local positions where the vertical distance from the reference level to the cloud-base will exceed 200 m.

Given (12) it is possible to calculate the pdf of the cloud-base height as a function of the pdfs of q_0 and T_0. We assume that the pressure is constant at the reference level. Expression 12 results in a pdf of the cloud-base height that is complicated in form. First, we use simulations drawing the specific humdity and temperature from non cross-correlated normal distributions as in (8). In the convective stratocumulus-topped boundary layer it is likely that there will be some degree of cross-correlation of the temperature and the specific humidity. This is considered at the end of this section. It is found that for p_0=1000 hPa, $\overline{T}_0$=290 K and $\overline{q}_0$=8.5 g kg^{-1}, the standard deviation of the cloud-base height is well represented by

$$\sigma_{CB} = \left\{(125\sigma_{T_0})^2 + (215\sigma_{q_0})^2\right\}^{\frac{1}{2}}. \qquad (13)$$

Simulations carried out using a range of input parameters p_0 [800-1000 hPa], $\overline{T}_0$ [275-295 K] and $\overline{q}_0$ [5.0-15.0 g kg^{-1}] show good agreement between the simulations and (13) especially when σ_{q_0} and σ_{T_0}

are small and $p_0 > 900$ hPa (i.e. cloud-base is lower than around 1500 m). Within the range of input parameters agreement is always better than 30%. This is demonstrated in Fig. 1 which shows a contour plot of σ_{CB} as a function of σ_{q_0} and σ_{T_0} from the simulations (solid contours) and from (13) (dotted contours) for the case where p_0=1000 hPa, $\overline{T}_0$=285 K and $\overline{q}_0$=8.5 g kg^{-1}.

Figure 2 shows a selection of cloud-base height pdfs (mean subtracted) resulting from the simulations described above. Overplotted are the predicted pdfs using the standard deviation predicted using (13). Excellent agreement between the simulated and predicted Gaussian pdfs is observed for all cases except for the case where p_0=850 hPa, σ_{q_0}=0.4 g kg^{-1} and σ_T=0.4 K. This latter case represents quite an extreme case (large fluctuations in T and q) for stratocumulus with complete cloud cover. Equation (13) is a fairly accurate predictor of the standard deviation of cloud-base height and the resulting pdfs are close to Gaussian. For two normally distributed variables X and Y, the linear combination $F = AX - BY$ has a standard deviation (zero covariance between X and Y) which is very similar in form to (13). Further, the standard deviation of F including the effects of covariance between X and Y is given by

$$\sigma_F = \left\{(A\sigma_X)^2 - 2AB\mathrm{Cov}(XY) + (B\sigma_Y)^2\right\}^{\frac{1}{2}}. \tag{14}$$

This would suggest that to include effects of covariance between the temperature and the specific humidity in the determination of the standard deviation of cloud-base height it might be possible to write

$$\sigma_{CB} = \left\{(A\sigma_{T_0})^2 - 2AB\mathrm{Cov}(T_0 q_0) + (B\sigma_{q_0})^2\right\}^{\frac{1}{2}} \tag{15}$$

with A=125 m K^{-1}. and B=215 m g^{-1} kg The reason for the negative sign preceeding the covariance term is because a positive covariance between temperature and specific humidity will reduce the variability of the cloud-base height and vice versa. To test this hypothesis simulations were carried out where the temperature and specific humidity are made to covary. Figure 3 shows the results of 400 simulations where σ_{T_0}, σ_{q_0} and the covariance of T and q were varied. The simulations were all made using p_0=900 hPa, $\overline{q_0}$=7.0 g kg^{-1} and $\overline{T_0}$= 280 K. It is clear that including the covariance term significantly improves the predictions with maximum errors in σ_{CB} reduced from around 40 m to 10 m. Notice also that there is a small bias (top right) with the predictions being around 7% lower than the simulations. This could be improved by including $\overline{T_0}$-dependent and $\overline{q_0}$-dependent prefactors in (13) and (15). Because the bias is small these were not considered here and would necessarily complicate the analysis.

In summary, a simple model has been developed to predict the variability of the cloud-base height in the boundary layer from fluctuating thermodynamic variables below cloud-base (temperature, specific humidity and their covariance). It has been shown that this model predicts distributions of cloud-base height that are close to Gaussian assuming that the sub-cloud variables are normally distributed and that the atmosphere between the reference level and the cloud-base is dry adiabatic. The standard deviations are predicted using a simple relationship, which was found to reproduce reasonably accurately the simulated standard deviations of cloud-base height. The Gaussian model of cloud-base height can then be used to predict *LWP* using an adiabatic model similar to that of CCW. The following sections use ground-based and aircraft observations of stratocumulus cloud to investigate the usefulness of such an approach in the prediction of the distribution of *LWP* in stratiform boundary layer clouds.

4 Observational validation

A range of observations is used to validate the simple model relationships discussed in the previous section. In section 4a ground-based microwave radiometer and ceilometer measurements from the First ICCP Regional Experiment (FIRE) are used to examine the link between fluctuations in cloud-base height and *LWP* (as predicted using CCW). In section 4b predictions of the standard deviation of cloud-base height from subcloud turbulent fluctuations in temperature and specific humidity are examined using aircraft data from the Met Office C-130 aircraft. Finally, in section 4c the relationship between the standard deviation of *LWP* and the subcloud turbulent fluctuations of temperature and specific humidity, which results from a combination of the CCW model and the simple adiabatic model to predict cloud-base variability, is examined using aircraft radiometric measurements of *LWP*. Data from four campaigns designed to measure stratocumulus cloud properties are used. Table 1 details the datasets used to examine each aspect. Due to instrumental or flight pattern logistics it is not possible to use data from every campaign to examine each of the aspects. Specific instrumental details are included in the following sections.

(a) Ground-based measurements of liquid water path and cloud-base variability

Observational results from the First ICCP Regional Experiment (FIRE) (Albrecht *et al.*, 1988) are used to investigate the relationships between cloud-base variability and *LWP* variability. A microwave radiometer and ceilometer were colocated on San Nicholas Island in the Pacific Ocean off the southern Californian coast for eighteen days during the intensive observational campaign. The site was chosen due to the large fraction of time that the Island is covered with low-level marine stratiform cloud (Fairall et al, 1990). The microwave radiometer (Hogg *et al.*, 1983) measured *LWP* continuously and was sampled every minute. The ceilometer (Schubert *et al.*, 1987) measured the height of the cloud-base and was sampled every 30 seconds.

Figure 4 shows time series of LWP and cloud-base height for the entire dataset (upper two panels). The diurnal variation of the liquid water path (e.g. Betts, 1990; Fairall *et al.*, 1990) is clearly observed (top panel). The cloud-base height also appears to exhibit a diurnal modulation with minima corresponding to maxima in *LWP* . The lower two panels show *LWP* and cloud-base height (solid lines) for a single 24-hour period (14 August 1987). Also shown is the inversion height obtained from radiosondes (solid circles, lowest panel). Shown plotted over the *LWP* data is the adiabatic *LWP* predicted from the cloud-base and the inversion height (Eq. (1)). The inversion height at any time is calculated using linear interpolation of the radiosonde inversion height measurements (shown as dashed line in lowest panel). The calculations are performed with $\Gamma_{adiab} = 2.6 \times 10^{-3}$ g m^{-4}, a mean value for the upper levels of the boundary layer from Albrecht *et al.* (1995b). For the duration of the FIRE observations Γ_{adiab} varied by no more than 10-20 percent. The error bars show the expected error for the adiabatic *LWP* given a measurement error of 50 m for the inversion height (the most likely source of error given the poor vertical resolution of radiosonde data). The adiabatic *LWP* agrees well with the measured *LWP* to within the estimated error over most of the period. It is also of particular interest to note that the small-scale fluctuations in the measured *LWP* are generally matched fairly closely by the adiabatic fluctuations suggesting that much of the variability in *LWP* is a result of fluctuations in cloud-base rather than cloud-top (which is significantly smoother).

Figure 5 shows a comparison of three-hourly mean *LWP* measurements against the corresponding adiabatic *LWP* from the radiosonde inversion and the ceilometer cloud-base height measurements. The error bars represent the estimated error in the microwave radiometer measurement (horizontal) and the derived adiabatic *LWP* (vertical, as in Fig. 4). Each data point represents a three-hour average where the cloud-base height did not undergo sudden large discrete jumps which would be suggestive of possible multiple cloud-layers, very thin stratocumulus with cumulus beneath, or drizzle events. The data show that the stratocumulus cloud in the FIRE dataset is reasonably well-modelled using the adiabatic relationship of (5), although there is some suggestion that the observed *LWP* means are in general lower than the modelled ones. The error bars show the errors in both observed and modelled estimates, which are estimated as 20 g m^{-2} for the observations. These data have been previously analysed by Albrecht et al. (1990) who showed that for much of the observational period the cloud liquid water path was close to the adiabatic value. They attributed relatively infrequent periods of subadiabaticity to the depletion of cloud water by drizzle. The choice of three-hour data sections was made for three reasons. First, given typical advective wind speeds of some 5-10 m s^{-1}, three-hourly sections are equivalent to approximately 50-100 km of advected cloud, which is similar to the size of a typical global model grid box. Second, significantly longer sections would be affected by diurnal gradients. Third, with ground-based data logged once every minute, enough data points were required to determine the standard deviations and means with reasonable accuracy.

As discussed in the introduction, the pdf of the *LWP* is of major importance to the modelling of radiative transfer through inhomogeneous stratocumulus cloud. The CCW model presents a form for the *LWP* pdf (Eqs. (4) and (7) above). Several sections of the time series of *LWP* and cloud-base height from the FIRE observations were chosen for comparison with the model. Each section was 7-10 hours in length (to obtain reasonable statistics for the generation of the pdf). Care was taken to take only sections of the dataset where a reasonable degree of statistical stationarity was present (i.e. not periods with strong gradients). The standard deviation of the cloud-base height was determined after first linearly detrending the data from the chosen period. The mean *LWP* was calculated from the data and used along with σ_{CB} to calculate the model pdf from (7). Observed and modelled pdfs are shown together with cloud-base height pdfs in Figs. 6a and 6b.

There is good agreement between the modelled and observed pdfs in most cases. For the case where the mean *LWP* is small and the cloud-base height distribution is fairly broad (Fig. 6b, top) both the observations and the model predict a positively skewed distribution. Model pdfs calculated using (4) (i.e. as a function of the mean cloud thickness rather than the mean *LWP*) were very similar although they were often offset along the *LWP* axis as a result of the errors in the determination of the inversion height.

Figure 7 shows measurements of the standard deviation of the *LWP* normalised with the standard deviation of the cloud-base height for the same three-hourly averages as in Fig. 5. In general the data agree well with the prediction from the adiabatic model which is represented by the dashed line, although the model generally underpredicts the standard deviations by around 10-30%. There are a number of possible reasons for this: (a) the measurement of cloud-base height standard deviation may be an underestimate of the true variation in cloud-base height; (b) the microwave radiometer may overestimate the standard deviation of the *LWP*; (c) sizeable small-scale fluctuations in the inversion height may exist and these would increase the true standard deviation of *LWP* even if the liquid water content is distributed adiabatically in the vertical; (d) regions of enhanced or depreciated liquid water content may exist within the cloud possibly as a result of drizzle formation or entrainment. It is difficult to suggest which of the above reasons is the most likely cause of the underprediction. What is important to note however, is that the adiabatic model appears to represent well the observed features of *LWP* variability and offers potential improvements to the representation of subgridscale structure of stratocumulus in climate models. Any improvement, of course, depends upon the ability to predict the variability in the cloud-base and it is this problem that the extension to the CCW model described in section 2 hopes to address.

The means of the observed and adiabatic *LWP* series are 104.3 and 100.1 g m^{-2} respectively, with standard deviations 89.7 and 83.5 g m^{-2}, which are in excellent agreement. Power spectra (Fig. 8) for the entire series of observed and adiabatic (modelled) *LWP* are in generally good agreement and follow a power law relationship with exponents of -1.51 $\pm$ 0.06 and -1.42 $\pm$ 0.11 for the observed and modelled spectra respectively (95% confidence limits). As with the liquid water content power spectra presented in Davis *et al.* (1996) the gradient of the *LWP* power spectra are less steep than the "-5/3" associated with fully developed homogeneous and isotropic 3D turbulence. It is unknown why the power in the modelled *LWP* at frequencies higher than around 3 hr^{-1} is greater than that in the observed *LWP* spectrum, although possible noise in the ceilometer data cannot be ruled out as a contributor. The error bars (shown for the power spectrum of observed *LWP* only) are calculated using 95% confidence limits based upon the variability in the periodogram according to Blackman and Tukey (1959). The inset in Fig. 8 shows the normalised cospectrum of the observed and modelled *LWP*, the normalised cospectrum being defined (for two series f_1 and f_2) as

$$\text{Normalised cospectrum} = \left\{ \frac{\mathrm{Co}(f_1, f_2)}{\mathrm{P}(f_1)^{\frac{1}{2}}\mathrm{P}(f_2)^{\frac{1}{2}}} \right\}^{\frac{1}{2}}. \tag{16}$$

where $\mathrm{Co}(f_1, f_2)$ is the cospectral density function and $\mathrm{P}(f_1)$ and $\mathrm{P}(f_2)$ are the power spectral density functions of f_1 and f_2 respectively. Thus for the cospectrum in Fig. 8, $f_1 = LWP_{obs}$ and $f_2 = LWP_{adiab}$. This function shows the square root of the ratio of the power associated with the correlation between the two series to the product of the power of the individual series. It is therefore a measure of the similarity in the fluctuations in the two series as a function of scale. If the observed and adiabatic series were identical then the normalised cospectrum would equal unity. Two completely uncorrelated series would lead to a normalised cospectrum of zero. At low freqencies it is clear that the observed and adiabatic *LWP* are in very good agreement. The similarity between the series falls off with increasing freqency which is consistent with the increasing noise in the adiabatic modelled *LWP*. On the 3 hr timescale (used to calculate means and standard deviations above) the normalised cospectrum has a value of around 0.8-0.9 which indicates that the adiabatic *LWP* series matches very well with the observed *LWP*. Further, it suggests that fluctuations in cloud-top height are of less importance than fluctuations in cloud base height in determining the *LWP* fluctuations on this time scale.

If we define z_{LWP} as the thickness that a cloud would have if the liquid water content within it was distributed adiabatically in the vertical, then

$$z_{LWP} = \left(\frac{2LWP}{\Gamma_{adiab}}\right)^{\frac{1}{2}}. \tag{17}$$

If the adiabatic model is a perfect one then $z_{LWP} = z_i - z_{CB}$. We also investigate how the fluctuations in z_{LWP} and z_{CB}, z_{LWP} and z_i compare. Figure 9 presents normalised cospectra of these series. The solid line indicates that at timescales longer than around 2 hours fluctuations in cloud thickness are well correlated with those in z_{LWP}. Fluctuations in cloud-base are also well correlated with fluctuations in z_{LWP}. At timescales for which cloud-top fluctuations are available (> 6 hours), the combination of fluctuations from both cloud-base and cloud-top (and their covariance) leads to normalised cospectra between z_{LWP} and $z_i - z_{CB}$ of 0.75-0.95. Thus, it is conceivable (although not directly testable with this dataset), that cloud-top fluctuations might be responsible for the discrepancy between z_{LWP} and the cloud-base only adiabatic model (i.e. z_{CB}) at shorter timescales. However, it appears that cloud-base fluctuations account for a sizeable fraction of the LWP variance. Figure 10 shows the variance in z_{LWP}, z_{CB}, z_i and $z_i - z_{CB}$ as a function of timescale. Certainly, the variance in $z_i - z_{CB}$ is close to that in z_{LWP} at all scales. The agreement is better when the cloud-top fluctuations are taken into account (the upper panel shows ratios between the variances). However, although the variance in the z_{CB} series alone is less than that in z_{LWP} at timescales longer than a few hours, the discrepancy is not enormous. These observations lend further support to a model of LWP fluctuations driven largely by fluctuations in cloud-base height.

These ground-based observations from FIRE cannot be used to examine fluctuations in cloud-top height on timescales shorter than approximately 6 hours, as this parameter was sampled using radiosonde ascents. In future, it is hoped that lidar measurements taken simultaneously above (nadir view) and below cloud (zenith view) will be useful in deriving the geometrical limits of cloud layers.

(b) Observations of the relationship between cloud-base height variability and fluctuating thermodynamic variables

Equation (15) presents a parameterisation of the relationship between the fluctuating variables (σ_{T_0}, σ_{q_0} and their covariance $\mathrm{Cov}(T_0 q_0)$) and the standard deviation of the cloud-base height. The relationship was derived for an adiabatic sub-cloud profile of temperature and humidity and would hold in this case providing that the vertical distance between the cloud-base height z_{CB} and the level z_0 and is at most 200 m. It was not possible to obtain simultaneous measurements of both turbulent variables and cloud-base height from the ground-based measurements during FIRE as the cloud-base height was rarely less than 200 m. In any case, turbulent statistics obtained in the surface-layer would probably not be representative of the well-mixed convective boundary-layer. Instead, it was decided that the relationship in (15) could be examined better using aircraft measurements. C-130 measurements from three observational campaigns are used in the analysis: FIRE (First ISCCP Regional Experiment, Albrecht *et al.* 1988), ASTEX (Atlantic Stratocumulus Transition Experiment, Albrecht *et al.* 1995a) and SATE-2 (South Atlantic Tropical Experiment). ASTEX observations were made in the Azores region in June 1992; SATE-2 observations were carried out in the extensive stratocumulus sheet off the coast of Namibia in September/October 1995. Details of temperature, humidity and liquid water instrumentation on the C-130 is presented in Rogers *et al.* (1995). In each case straight and level runs were carried out both in and below extensive stratocumulus cloud sheets. In all cases used here the stratocumulus cloud cover was total. During most of the flights at least one run was carried out a short distance (<200 m) below cloud-base with another run in continuous cloud along the same air-track. Assuming that the adiabatic model of in-cloud liquid water content holds, then a liquid water content q_L time series measured during a constant-level run in continuous cloud can be used to derive the standard deviation of the cloud-base height using

$$q_L = \Gamma_{adiab}\left(z_{aircraft} - z_{CB}\right). \tag{18}$$

This can be compared to inferred values of the standard deviation of cloud-base height from a sub-cloud run using both (12) and the parameterisation equation (15). Figure 11 shows the results from a number of such analyses from continuous stratocumulus cloud during FIRE (solid circles), ASTEX (open triangles) and SATE-2 (asterisks). Here, the standard deviation derived using the in-cloud run is plotted against that from the sub-cloud run. Despite the scatter in the results it appears that both methods (sub-cloud and in-cloud) predict cloud-base height standard deviations that are broadly similar (to within 30%). The rms difference between in-cloud and sub-cloud predictions is 14.5 m with a mean bias of -2.6 m. The best estimate of the cloud-base standard deviation is taken as the mean of these two estimates. This is plotted against the parameterised cloud-base standard deviation from Eqs. (13) (no consideration of the covariance of temperature and humidity) and (15) (covariance between temperature and humidity included) in Fig. 12.

The rms error between observed and predicted σ_{CB} is 11.9 m without inclusion of the covariance term and reduces to 8.8 m when covariance is included. The mean biases in cloud base standard deviation (observed-predicted) are 3.4 m and -0.2 m respectively. The results suggest (without direct observations of cloud-base height) that the standard deviation of the cloud-base height is indeed related as expected to the sub-cloud variability in the temperature and humidity. The lack of any strong bias in the results is also encouraging. The error in the predicted σ_{CB} largely results from sampling errors in the turbulent variance terms σ_{T_0}, σ_{T_0} and $\mathrm{Cov}(T_0 q_0)$. An error analysis of (15) gives errors in the predicted σ_{CB} which range from 5-25 m given typical errors in σ_{T_0} and σq_0 of between 10-50%. Such sampling errors commonly arise in the measurement of scalar variances and can be estimated using integral scale arguments (e.g. Lenschow and Stankov 1986). The results suggest that the cloud-base height standard deviation is reasonably well predicted using the derived parameterisations and that inclusion of the covariance of temperature and humidity results in slightly more accurate predictions.

It is of interest to examine the relative magnitudes of the three contributing terms in (15). Contributions of the temperature fluctuation term (T term $\equiv (A\sigma_{T_0})^2$), the specific humidity fluctuation terms (q term $\equiv (B\sigma_{q_0})^2$) and the covariance term (Covar. term $\equiv -2AB\mathrm{Cov}(T_0 q_0)$) to the variance of the cloud-base height (Table 2) show that for each of the three datasets the variability in specific humidity is the major contribution to the cloud-base variability. The relative contribution of the covariance term is smallest in FIRE and SATE-2 but is relatively important in the ASTEX dataset. Note also that the covariance between temperature and specific humidity tends to result in an *increase* in the cloud-base variance for all three datasets. This is because at lengthscales larger than approximately 1-2 km, the temperature and specific humidity are generally negatively correlated. Figure 13 shows ensemble averaged power spectra $S_T(k)$ and $S_q(k)$ of temperature and specific humidity from the three datasets. Additional data are included from the MAST field campaign (Durkee et al. 2000). All runs were taken below 8/8 stratocumulus cloud. Note that both T and q power spectral densities exhibit a power law relationship with an approximate (-5/3) exponent (shown by dashed line). The lower panel shows the cospectral density $(\mathrm{Co}_{T,q}(k)/(S_T(k)S_q(k))^{1/2})$ as a function of wavenumber k, demonstrating the negative correlation between T and q at lengthscales longer than 1-2 km. A generally negative $T-q$ correlation has also been observed by, amongst others, Williams et al. (1996) in the tropical warm pool boundary layer (see their Fig. 7), who attribute the behaviour to the effects of downward entrainment of warm/dry into the boundary layer. Other observations of the negative correlation have been made (e.g. Donelan and Miyake 1973; Wyngaard and LeMone 1980). The positive correlation between T and q at short lengthscales results from the upwards transport of moist air in convectively buoyant updraughts. Contribution from entrainment most likely affects all lengthscales but the effects of buoyant thermals swamps out the effect at short wavelengths. In calculating the cloud-base height standard deviation in Eqn. 15, the covariance term is largely positive because the total contribution from all scales to the $T-q$ covariance is dominated by fluctuations on lengthscales larger than 1-2 km.

As an example of the cloud-base height estimations using the two methods, Fig. 14 shows cloud-base height pdfs predicted using the two methods. Each cloud-base height time series was linearly detrended to remove effects of large-scale gradients. The upper panel shows a data from a well-mixed shallow boundary layer and the lower panel data from a decoupled boundary layer. Both examples are taken from ASTEX Lagrangian cases documented previously by Bretherton and Pincus (1995). Although there are some differences in the two measurements of the pdf the general forms and widths are similar.

An important feature of Fig. 12 is that, in general, the largest values of σ_{CB} are found for the ASTEX data, with smaller values typically observed for the FIRE and SATE-2 observations. Table 3 gives boundary layer depths and cloud-base standard deviations from the three campaigns. A two-sample t-test for populations with unknown standard deviations shows that the estimated mean boundary layer depth during ASTEX was greater than that during both FIRE and SATE-2 at the 95% confidence level. The boundary layer depth during SATE-2 was greater than that during FIRE only at the 67% confidence level. The standard deviation of cloud-base height was statistically significantly greater during ASTEX than during FIRE (95% confidence level) and during SATE-2 (80% confidence level). The standard deviation of cloud-base height during SATE-2 was significantly greater than that in FIRE

(80% confidence level). Figure 15 shows the standard deviation of cloud-base height plotted against the boundary layer depth for all the FIRE, ASTEX and SATE-2 cases. Also plotted is the least-squares best fit which is given by

$$\sigma_{CB} = 0.051(\pm 0.016)z_i - 8.4(\pm 16.9) \tag{19}$$

with correlation coefficient $r^2 = 0.56$, and the errors in (19) given at the 95% confidence level. Thus, it can be concluded that boundary layers during ASTEX were generally deeper, and cloud-base standard deviations generally larger, than in FIRE and SATE-2. Davis *et al.* (1996) (their Fig. 7) show how the ensemble-averaged power spectral density of liquid water content fluctuations was greater in ASTEX than in FIRE . Larger variance in liquid water content, in the adiabatic framework, is consistent with higher variance in cloud-base height. Note however, that because σ_{CB} follows a power law scaling relationship (not shown), its standard deviation increases as the scale increases. Thus, Eqn. 19 is applicable only at the scale of the observations (60-90 km aircraft run length). For example, it is not possible to compare these results directly with large eddy simulations (LES), as these usually have domain sizes considerably smaller than the aircraft run lengths. Ground-based observations from FIRE show that z_{CB} exhibits Kolmogorov-type scaling (approximately "-5/3" slope). From Parseval's theorem, one would therefore expect the standard deviation in z_{CB} to scale with (length scale)$^{1/3}$. Thus, cloud-base height standard deviations over typical LES domains of 4-8 km are likely to be 35-50% of those over 60-90 km domains.

The results shown here suggest a possible framework for the prediction of cloud-base variability from sub-cloud turbulent variables. With further improvements in observational capability (for example by airborne radiometric ceilometer measurements) such direct and quantitative observations will be possible.

(c) Aircraft validation of the relationship between LWP variability and turbulent fluctuations of temperature and humidity

The relationship between the cloud-base variability and *LWP* variability has been examined observationally in section 4a. Here, we use radiometric aircraft observations of *LWP* and subcloud measurements of the turbulent fluctuations of temperature and specific humidity to validate the model relationship between turbulence and *LWP* variability. Equations (6) and (15) are combined to give:

$$\sigma_{LWP} = \sqrt{2}\Gamma_{adiab}{}^{\frac{1}{2}}\overline{LWP}^{\frac{1}{2}} \left\{ (A\sigma_{T_0})^2 - 2AB\mathrm{Cov}(T_0 q_0) + (B\sigma_{q_0})^2 \right\}^{\frac{1}{2}} \tag{20}$$

where A=125 m K^{-1} and B=215 m g^{-1} kg. Liquid water path is retrieved using a two-channel airborne microwave radiometer (Guillou *et al.* 1996) operating at 89 and 157 GHz which can view either in nadir or zenith directions. The *LWP* retrieval algorithm is described in detail in English (1995) and can be used either below cloud (zenith view) or above cloud (nadir view). The sampling strategy for the analysis presented here was to carry out a straight and level run a short distance below cloud-base to obtain temperature and humidity measurements. In some cases this run was also used to derive the liquid water path of the cloud above (zenith view). In other cases a second run above cloud (nadir view) was used to derive the *LWP* measurement. In all cases where two runs were used the aircraft sampled in a Lagrangian sense (i.e. the runs were centred on a fixed air position). Data were taken from three campaigns: ASTEX, SATE-2 (described previously) and the Monterey Area Ship Tracks Experiment. MAST was carried out in June 1994 in the extensive sheets of stratocumulus that develop close to the Californian coast. The airborne microwave radiometer was not fitted during FIRE and so no *LWP* data are available from this campaign. The aircraft runs used were typically 10-15 minutes in duration, and covered a horizontal distance of 60-90 km. This is comparable to the ground-based sampling length used in section 4(a).

Figure 16 shows the observed *LWP* standard deviation against that predicted using (20). In calculating the predicted standard deviation the observed mean liquid water content was used. The dotted line denotes perfect agreement. There is a considerable degree of scatter in the results (correlation coefficient, r^2=0.90) but the gradient of the least-squares fit suggests that the model reproduces the observed *LWP* standard deviations with small overall bias.

5 Discussion

The FIRE experiment has provided data to validate the CCW adiabatic model of *LWP* distributions. Observed *LWP* distributions have been shown to agree very well with those predicted given the mean liquid water path and the standard deviation of cloud-base. In most cases the cloud-base pdf is fairly close to a normal distribution which is the assumption necessary for the prediction of the pdf of *LWP*. The observed pdf widths (quantified by the standard deviation) are in general 10-30% greater than those predicted using the model. Several reasons, some physical, some instrumental, were suggested for this.

The second set of observations was taken from aircraft data below and in-cloud to attempt to explain the variability in cloud-base as a function of the fluctuations in temperature and humidity. Although no direct observations of cloud-base height were available from the aircraft, it was possible to infer cloud-base height from horizontal distributions of liquid water content. The cloud-base height pdfs thus derived were in good agreement with those predicted using an adiabatic model of the sub-cloud atmosphere between the aircraft level and the cloud-base. The results suggest that the turbulent variances of temperature and humidity could potentially be used to infer cloud-base variability and hence the liquid water path probability distributions in marine stratocumulus. Further, more direct measurements will allow a more direct and quantitative assessment of this. Stratocumulus cloud inhomogeneity is clearly linked to inhomogeneity in temperature and humidity fields: it may be possible to develop prognostic equations for the evolution of temperature and humidity variance (and their covariance). However, to do this will require knowledge and understanding of the causes and effects of higher order terms in the variance budget equations. Given that these terms are likely to have effects over a wide range of different spatial scales, this presents a particularly difficult challenge.

The effect of *LWP* variability upon the reflection and transmission of short-wave radiation through inhomogeneous cloud is currently a major focus of research. Most radiative transfer routines currently used in large-scale numerical weather prediction and climate models do not consider subgrid variability within stratiform cloud at all (e.g. Slingo 1989) and it has been shown that this can result in typical errors of 0.09 (15%) in a cloud albedo of 0.6 (Cahalan *et al.* 1994). Given that the globally-averaged stratocumulus/stratus cloud cover is around 29% (Klein and Hartmann 1993) the neglection of internal homogeneity in stratiform cloud would result in substantial short-wave forcing errors. In current climate models this is often compensated for by model clouds with unrealistically small liquid water contents or cloud fractions (Bushell and Martin 1999).

Further work is required to develop parameterisations of stratocumulus cloud inhomogeneity for inclusion in large-scale numerical models. In such models, radiative transfer calculations already require a substantial fraction of the total computing power required. It may well be possible to derive cloud radiative transfer characteristics as a function of inhomogeneity parameters such as cloud-base standard deviation to provide a more realistic representation of stratocumulus clouds in large-scale models.

ACKNOWLEDGEMENTS

The authors wish to thank the staff of Meteorological Research Flight, the C-130 RAF aircrew and all of the other participants and organisers of the FIRE, ASTEX, MAST and SATE-2 projects. We are grateful to NASA Langley DAAC Staff for the provision of FIRE ground-based microwave radiometer/ceilometer/radiosonde data.

References

Albrecht, B. A., Randall, D. A., and Nicholls, S. N. (1988): Observations of marine stratocumulus during FIRE. *Bull. Am. Meteor. Soc.*, **69**, 618–626.

Albrecht, B. A., Fairall, C. W., Thomson, D. W., White, A. B., Snider, J. B. and Schubert, W. H. (1990): Surface-based remote sensing of the observed and adiabatic liquid water content of stratocumulus clouds. *Geophys. Res. Lett.*, **17**, 89–92.

Albrecht, B. A., Bretherton, C. S., Johnson, D. W., Schubert, W. H., and Frisch, A. S. (1995a): The atlantic stratocumulus transition experiment - ASTEX. *Bull. Am. Meteorol. Soc.*, **76**, 889–908.

Albrecht, B. A., Jensen, M. P., and Syrett, W. J. (1995b): Marine boundary layer structure and fractional cloudiness. *J. Geophys. Res.*, **100**(D7), 14209–14222.

Austin, P., Wang, Y., Pincus, R., and Kujala, V. (1995): Precipitation in stratocumulus clouds: observations and modelling results. *J. Atmos. Sci.*, **52**, 2329–2352.

Berry, E. X. and Reinhardt, R. L. (1974): An analysis of cloud drop growth by collection: Part II. single initial distributions. *J. Atmos. Sci.*, **31**, 1825–1831.

Betts, A. K. (1990): Diurnal variation of California coastal stratocumulus from two days of boundary layer soundings. *Tellus*, **42A**, 302–304.

Blackman, R. B. and Tukey, J. W. (1959): *The measurement of power spectra*, Dover Publications Ltd, New York, NY 10014, USA.

Brenguier, J. L., Chuang, P. Y., Fouquart, Y., Johnson, D. W., Parol, F., Pawlowska, H., Pelon, J., Schuller, L., Schroder, F., and Snider, J. (2000): An overview of the ACE-2 Cloudy-Column closure experiment. *Tellus*, **52B**, 815–827.

Bushell, A. C. and Martin, G. M. (1999): The impact of vertical resolution on GCM simulations of marine stratocumulus. *Clim. Dyn.*, **15**, 293–318.

Cahalan, R. F., Ridgway, W., Wiscombe, W. J., Bell, T. L., and Snider, J. B. (1994): The albedo of fractal stratocumulus clouds. *J. Atmos. Sci.*, **51**, 2434–2455.

Considine, G., Curry, J. A., and Wielicki, B. (1997): Modeling cloud fraction and horizontal variability in marine boundary layer clouds. *J. Geophys. Res.*, **102**(D12), 13517–13525.

Davis, A., Marshak, A., Wiscombe, W., and Cahahlan, R. (1996): Scale invariance of liquid water distributions in marine stratocumulus. Part I: Spectral properties and strationarity issues. *J. Atmos. Sci.*, **53**, 1538–1558.

Donelan, M. and Miyake, M. (1973): Spectra and fluxes in the boundary layer of the trade-wind zone. *J. Atmos. Sci.*, **30**, 444-464.

Durkee, P. A., Noone, K. J., Bluth, R. T. (2000): The Monterey ship track experiment. *J. Atmos. Sci.*, **57**, 2523–2541.

English, S. J. (1995): Airborne radiometric observations of cloud liquid-water emission at 89 and 157 ghz: Application to retrieval of liquid water path. *Quart. J. Roy. Meteorol. Soc.*, **121**, 1501–1524.

Fairall, C. W., Hare, J. E., and Snider, J. B. (1990): An eight-month sample of marine stratocumulus cloud fraction, albedo, and integrated liquid water. *J. Clim.*, **3**, 847–864.

Gerber, H., Arends, B. G., and Ackerman, A. S. (1994): New microphysics sensor for aircraft use. *Atmos. Res.*, **31**, 235–252.

Guillou, C., English, S. J., Prigent, C. and Jones, D. C. (1996): Passive microwave airborne measurements of the sea surface response at 89 and 157 GHz. *J. Geophys. Res.*, **101**(C2), 3775–3788.

Hignett, P. and Taylor, J. P. (1996): The radiative properties of inhomogeneous boundary layer cloud: observations and modelling. *Quart. J. Roy. Meteorol. Soc.*, **122**, 1341–1364.

Hogg, D. C., Guiraud, F. O., Snider, J. B., Decker, M. T. and Westwater, E. R. (1983): A steerable dual-channel microwave radiometer for measurement of water vapour and liquid in the atmosphere. *J. Appl. Meteorol.*, **22**, 789–806.

Klein, S. A. and Hartmann, D. L. (1993): The seasonal cycle of low stratiform clouds. *J. Climate*, **6**, 1588–1606.

Larson, V. E., Wood, R., Field, P. R., Golaz, J.-C., Vonder Haar, T. H., and Cotton, W. R. (2000): Systematic biases in the microphysics and thermodynamics of numerical models that ignore subgrid-scale variability. *J. Atmos. Sci.*, in press.

Lenschow, D. H. and Stankov, B. B. (1986): Length scales in the convective boundary layer. *J. Atmos. Sci.*, **43**, 1190–1209.

Liou, K. N. and Ou, S. C. (1989): The role of cloud microphysical processes in climate: An assessment from a one-dimensional perspective. *J. Geophys. Res.*, **94**, 8599–8607.

Marshak, A., Davis, A., Wiscombe, W., and Cahalan, R. (1998): Radiative effects of sub-mean free path liquid water variability observed in stratiform clouds. *J. Geophys. Res.*, **103**(D16), 19557–19567.

Nicholls, S. and Leighton, J. (1986): An observational study of the structure of stratiform cloud sheets: Part I. structure. *Quart. J. Roy. Meteorol. Soc.*, **112**, 431–460.

Pawlowska, H., Brenguier, J-L., and Burnet, F. (2000): Microphysical properties of stratocumulus clouds. *Atmos. Res.*, in press.

Pincus, R., and Bretherton, C. S. (1995): Cloudiness and marine boundary layer dynamics in the ASTEX Lagrangian Experiments. Part I: Synoptic setting and vertical structure. *J. Atmos. Sci.*, **52**, 2707–2723.

Pincus, R., and Klein, S. A. (2000): Unresolved spatial variability and microphysical process rates in large scale models. *J. Geophys. Res.*, in press.

Rogers, D. P., Johnson, D. W., and Friehe, C. A. (1995): The stable internal boundary layer over a coastal sea. Part I: Airborne measurements of the mean and turbulence structure. *J. Atmos. Sci.*, **52**, 684–696.

Rotstayn, L. D., (2000): On the "tuning" of autoconversion parameterizations in climate models. *J. Geophys. Res.*, **105**, 15,495–15,507.

Schubert, W. H., Cox, S. K., Ciesielski, P. E., and Johnson-Pasqua, C. M. (1987): Operation of a ceilometer during the fire marine stratocumulus experiment. *Colorado State University Atmospheric Science Pap.*, 420, 101pp.

Slingo, A., Nicholls, S., and Schmetz, J. (1982): Aircraft observations of marine stratocumulus during JASIN. *Quart. J. Roy. Meteorol. Soc.*, **108**, 833–856.

Slingo, A. (1989): A GCM parameterization for the shortwave properties of water clouds. *J. Atmos. Sci.*, **46**, 1419–1427.

Stephens, G. L. (1986): Radiative transfer in spatially heterogeneous, two-dimensional anisotropically scattering media. *J. Quant. Spectrosc. Radiat. Transfer*, **36**, 51–67.

Tripoli, G. J. and Cotton, W. R. (1980): A numerical investigation of several factors contributing to the observed variable density of deep convection over south Florida. *J. App. Meteorol.*, **19**, 1037–1063.

Williams, A. G., Kraus, H. and Hacker, J. (1996): Transport Processes in the tropical warm pool boundary layer. Part I: Spectral Composition of Fluxes. *J. Atmos. Sci.*, **53**, 1187–1202.

Wyngaard, J. C., and LeMone, M. A. (1980): Behaviour of the refractive index structure parameter in the entraining convective boundary layer. *J. Atmos. Sci.*, **37**, 1573–1585.

Table 1: Details of observational field campaigns used in this study. Due to instrumental limitations, or the nature of the aircraft flight patterns, not all campaigns can be used to examine each aspect presented in this study. Each campaign took place over the sea in regions where low-level boundary layer cloud is present for much of the time.

Table 2: Dataset-mean contribution of temperature and specific humidity fluctuations and covariance to the variance of cloud-base height derived using (15) differentiated according to dataset (FIRE, ASTEX and SATE-2). The number of runs used to derive the means n is also shown.

Table 3: Dataset-mean boundary layer depth and cloud-base height standard deviation. The values in brackets are standard deviations of the values from the n runs for each of the FIRE, ASTEX and SATE-2 datasets. The cloud-base height standard deviation increases with increasing boundary layer depth.

Figure 1: Contour plot of the standard deviation of cloud-base height [m] as a function of the standard deviations of temperature and specific humidity. The solid lines are results from the simulations and the dashed lines are those predicted using 13). All data refer to the case where p_0=1000 hPa, $\overline{T}_0$=285 K and $\overline{q}_0$=8.5 g kg^{-1}.

Figure 2. Probability density functions of cloud-base height (with mean subtracted) from the simulations (solid) and predicted using (13) for a range of input parameters. Good agreement between the analytical pdfs and the simulated ones is obtained in all cases apart from the case where p_0=850 hPa, $\overline{q}_0$=0.4 g kg^{-1} and $\overline{T}_0$=0.4 K.

Figure 3: Results of 400 simulations where σ_{T_0}, σ_{T_0} and the covariance of T_0 and q_0 were varied. The upper left-hand plot shows σ_{CB} predicted using (13) (i.e. no covariance term in the prediction equation) against the simulated σ_{CB}. The upper right-hand plot shows the same comparison but using (15) (i.e. the covariance term is included in the prediction). Dotted lines indicate perfect agreement. The lower two plots show the respective errors (predicted-simulated) against the covariance ($\mathrm{Cov}(T_0 q_0)$).

Figure 4: Time series of *LWP* and cloud-base height for the entire FIRE dataset (upper two panels) and for a single day (lower two panels). The adiabatic *LWP* is also plotted (with estimated error bars - see text) and shows good agreement in both the small-scale fluctuations and the longer-term fluctuations. The radiosonde data used to derive the inversion height is shown on the lowest panel.

Figure 5: Three-hour means of observed and adiabatic *LWP*. Observational error bars are shown as 20 g m^{-2}.

Figure 6a,b: Example observed and modelled pdfs of cloud-base height (left) and *LWP* (right) from the FIRE dataset. The dashed lines show the fitted normal distribution for the cloud-base height (left) and the calculated adiabatic model *LWP* distribution (right).

Figure 7: Three-hour means of the standard deviation of *LWP* normalised with the cloud-base height standard deviation plotted against the mean *LWP*. The dashed line shows the prediction from the adiabatic model.

Figure 8: Power spectrum of observed (solid circles) and modelled (triangles) *LWP* time series from FIRE. Inset shows normalised cospectrum (see text for definition) of observed and modelled *LWP* for which a value of unity indicates that the observed and modelled *LWP* correlate perfectly.

Figure 9: Normalised cospectra of $z_{CB}; z_{LWP}$ (dashed), $z_i; z_{LWP}$ (dotted) and $z_i - z_{CB}; z_{LWP}$ (solid).

Figure 10: Main panel: Mean variance as a function of scale for z_{LWP} (circles), z_{CB} (dashed), z_i (dotted) and $z_i - z_{CB}$ (solid). Upper panel: Ratio of the variances of z_{CB}, z_i and $z_i - z_{CB}$ to the variance in z_{LWP}, as a function of timescale.

Figure 11: Standard deviation of cloud-base height inferred from sub-cloud and in-cloud aircraft runs during FIRE (solid circles) and ASTEX (open triangles). Reasonably good agreement is observed suggesting that the cloud-base is reasonably well-predicted using the sub-cloud adiabatic model.

Figure 12: Cloud-base height standard deviations (taken to be the mean of the standard deviations from the sub-cloud and in-cloud runs) plotted against those predicted using (13) (no covariance term, top) and (15) (covariance term included, bottom). Better agreement is observed when the covariance of the temperature and the humidity is included.

Figure 13. Power spectra of temperature T (upper panel) and specific humidity q (centre panel) from sub-cloud runs during FIRE, ASTEX, SATE-2 and MAST. Cospectra normalised with the product of the two power spectra (lower panel). Each dataset is an ensemble average taken from 14-23 aircraft runs. Both T and q show power law relationships with no spectral gap and a near-constant exponent (dashed line shows -5/3 slope). The correlation between T and q is positive at small scales and negative at large scales indicating that transport by convective thermals dominates the correlation at scales smaller than 1-2 km, and that slow downward entrainment of warm, dry air from above cloud-base dominates at larger scales.

Figure 14: Cloud-base height example pdfs derived from sub-cloud and in-cloud aircraft runs from a well mixed boundary layer (top) and a decoupled boundary layer (bottom). Both sets of data are from ASTEX Lagrangian cases documented previously in Bretherton and Pincus (1995).

Figure 15: Standard deviation of cloud-base height plotted against boundary layer depth from all FIRE (solid circles), ASTEX (triangles) and SATE-2 (asterisks) aircraft cases. The best fit straight line is also shown.

Figure 16: Observed standard deviation of LWP agianst that predicted using subcloud turbulent variables.

Table 1:

	Campaign			
	FIRE	ASTEX	MAST	SATE-2
Location:	E. Pacific	N. Atlantic	E. Pacific	S. Atlantic
Date:	June/July 1987	June 1992	June 1994	Sept/Oct 1995
Aspects examined:				
LWP/z_{CB} variability?	Y	N	N	N
z_{CB} standard deviation?	Y	Y	N	Y
(T, q) power/co-spectra?	Y	Y	Y	Y
$LWP/(T, q)$ variability?	N	Y	Y	Y

Table 2:

		Dataset mean value of terms contributing to σ_{cb}^2		
Dataset	n	T term [m^2]	q term [m^2]	Covar. term [m^2]
FIRE	15	416	776	245
ASTEX	11	637	2134	1031
SATE-2	10	340	1935	199

Table 3:

Dataset	n	$\overline{z_i}$ [m]	$\overline{\sigma_{CB}}$ [m]
FIRE	15	863 (130)	33.8 (12.5)
ASTEX	11	1309 (436)	58.6 (31.0)
SATE-2	10	950 (239)	43.2 (18.5)

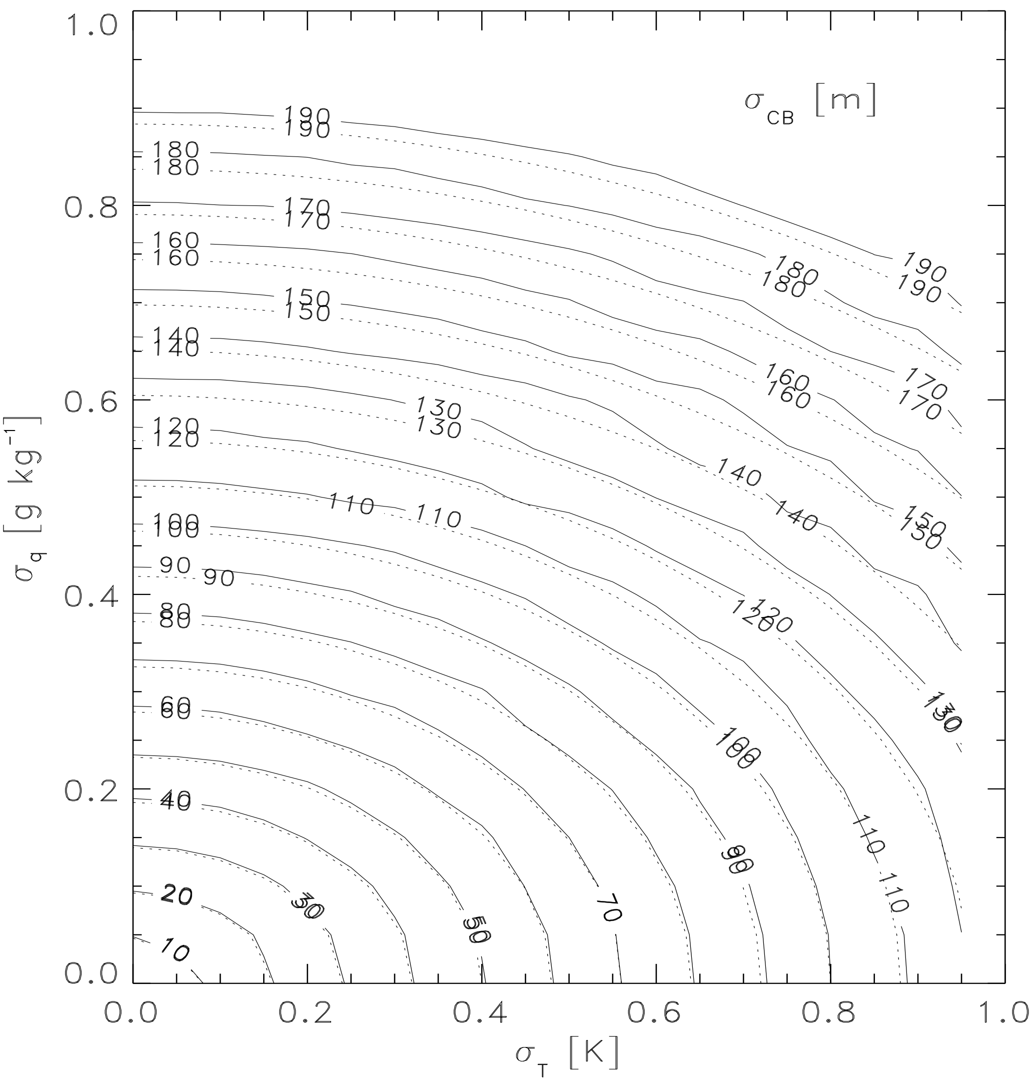

σ_{CB} [m]
σ_q [g kg^{-1}]
σ_T [K]
0.0
0.2
0.4
0.6
0.8
1.0
10
20
30
40
50
60
70
80
90
100
110
120
130
140
150
160
170
180
190

Figure 1:

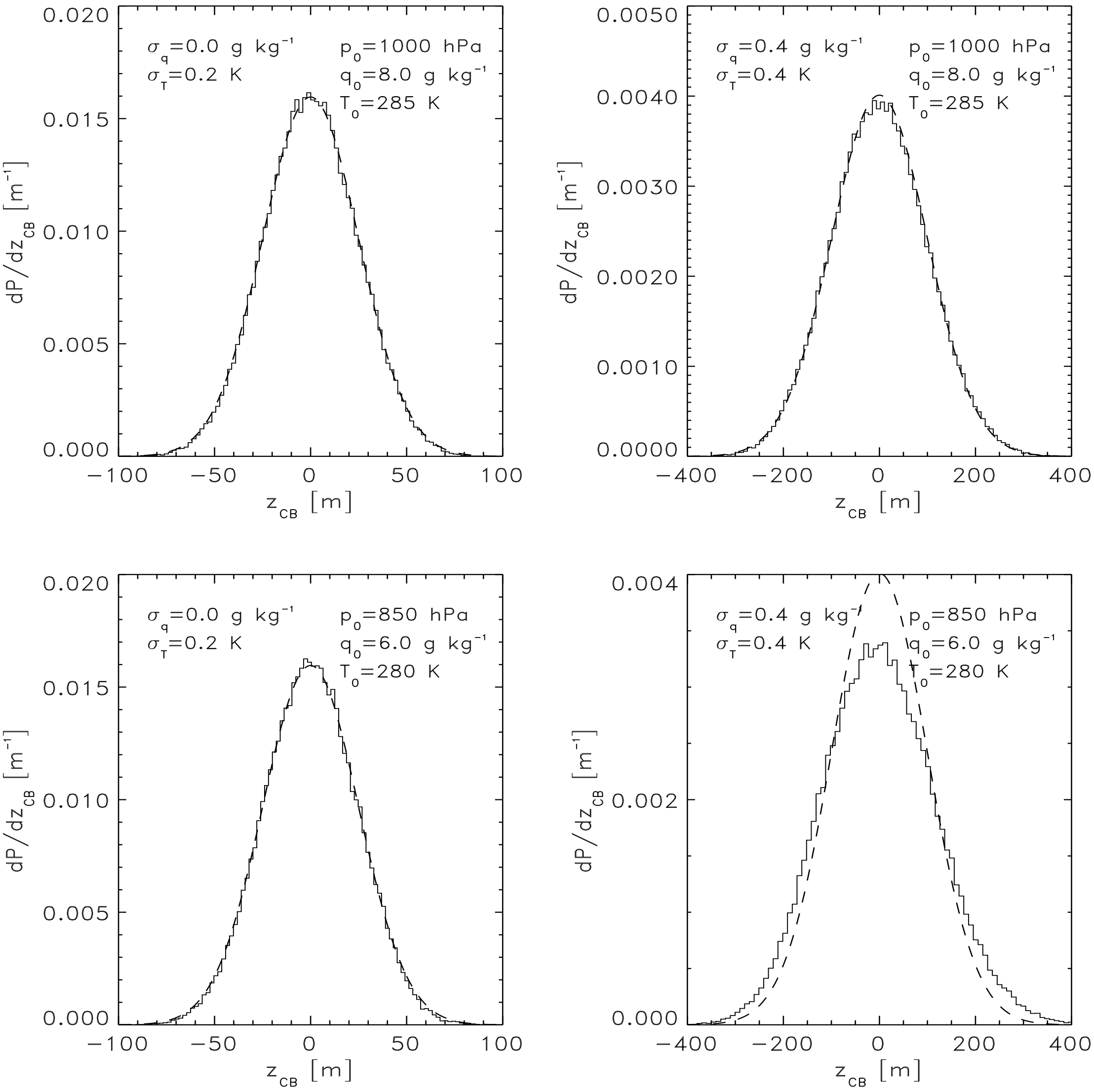

σq=0.0 g kg⁻¹
σT=0.2 K
p0=1000 hPa
q0=8.0 g kg⁻¹
T0=285 K
dP/dzCB [m⁻¹]
zCB [m]
σq=0.4 g kg⁻¹
σT=0.4 K
p0=1000 hPa
q0=8.0 g kg⁻¹
T0=285 K
σq=0.0 g kg⁻¹
σT=0.2 K
p0=850 hPa
q0=6.0 g kg⁻¹
T0=280 K
σq=0.4 g kg⁻¹
σT=0.4 K
p0=850 hPa
q0=6.0 g kg⁻¹
T0=280 K

Figure 2:

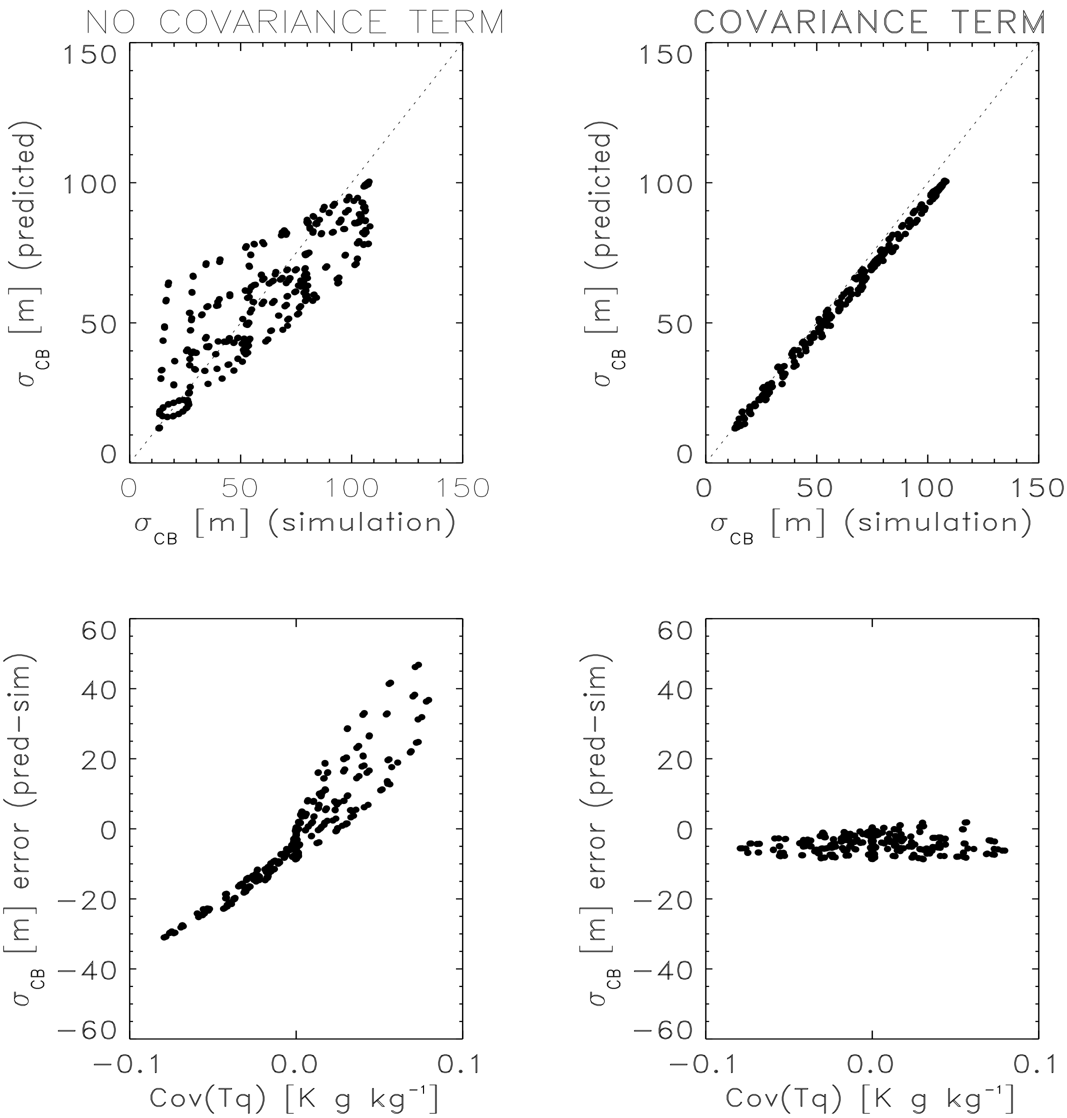
NO COVARIANCE TERM
COVARIANCE TERM
150
100
50
0
0
50
100
150
σ_{CB} [m] (predicted)
σ_{CB} [m] (simulation)
60
40
20
0
−20
−40
−60
−0.1
0.0
0.1
σ_{CB} [m] error (pred−sim)
Cov(Tq) [K g kg^{-1}]

Figure 3:

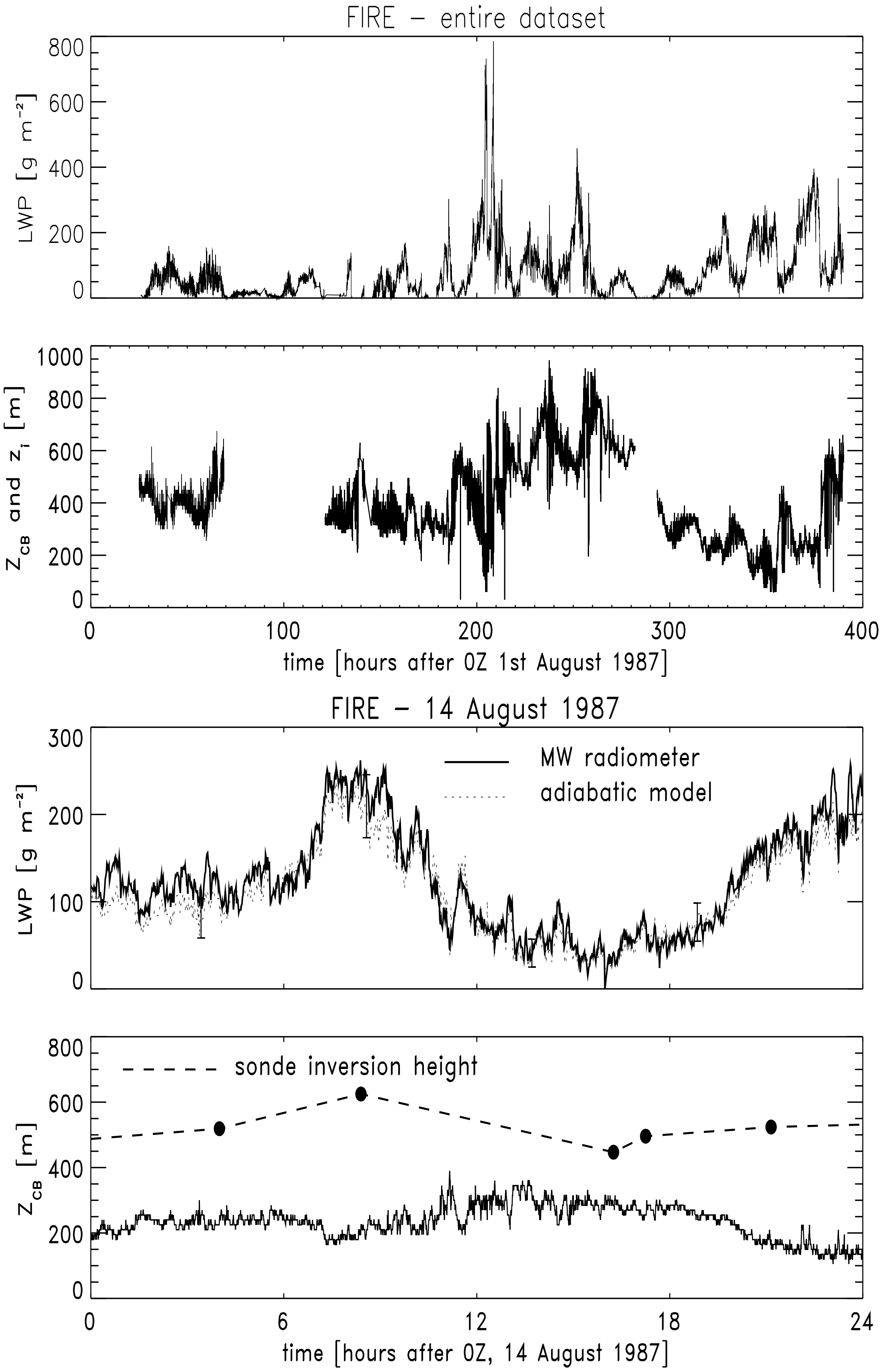

FIRE – entire dataset
LWP [g m⁻²]
0
200
400
600
800
Z_CB and z_i [m]
0
200
400
600
800
1000
0
100
200
300
400
time [hours after 0Z 1st August 1987]
FIRE – 14 August 1987
LWP [g m⁻²]
0
100
200
300
MW radiometer
adiabatic model
Z_CB [m]
0
200
400
600
800
sonde inversion height
0
6
12
18
24
time [hours after 0Z, 14 August 1987]

Figure 4:

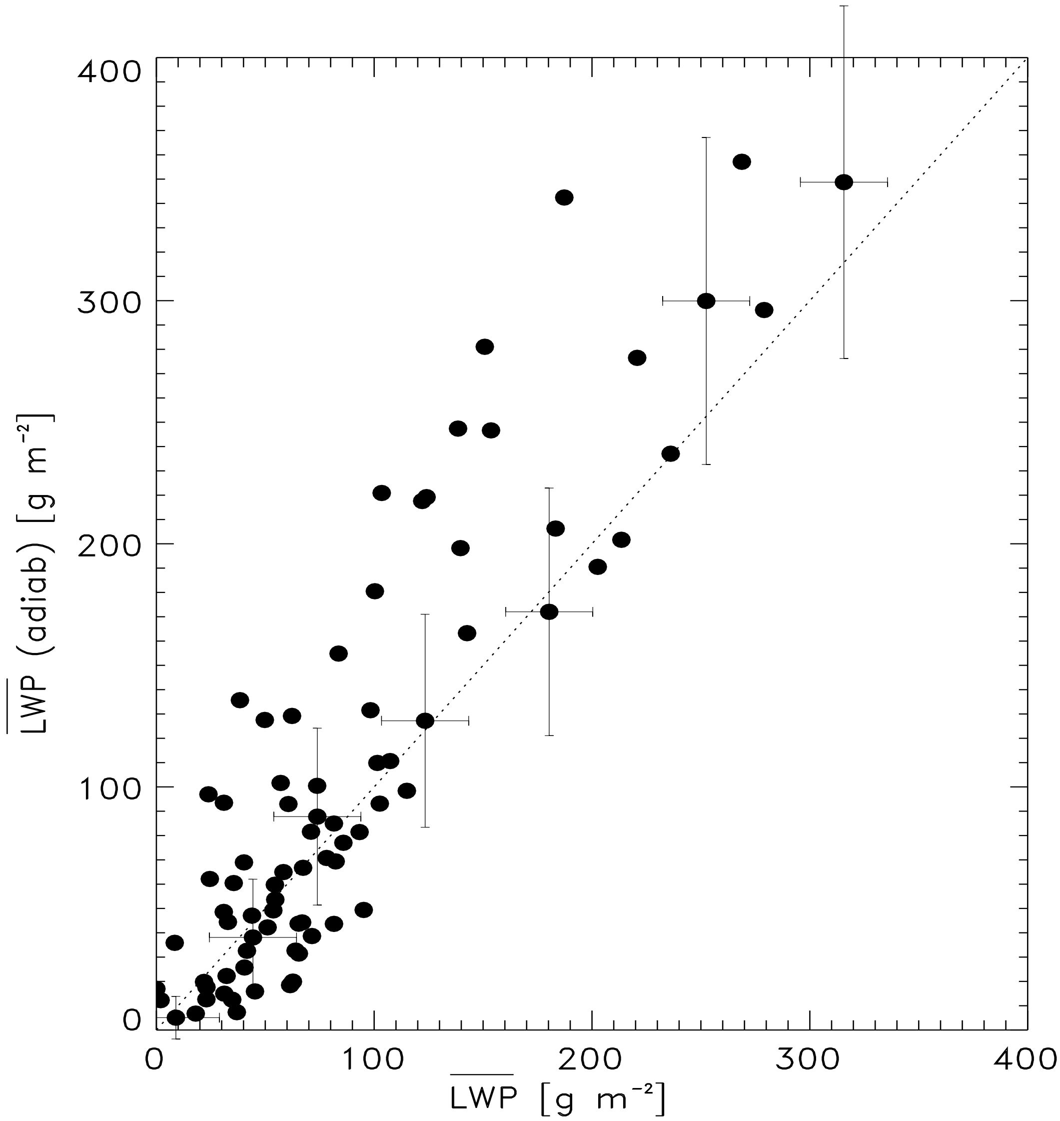

Figure 5:

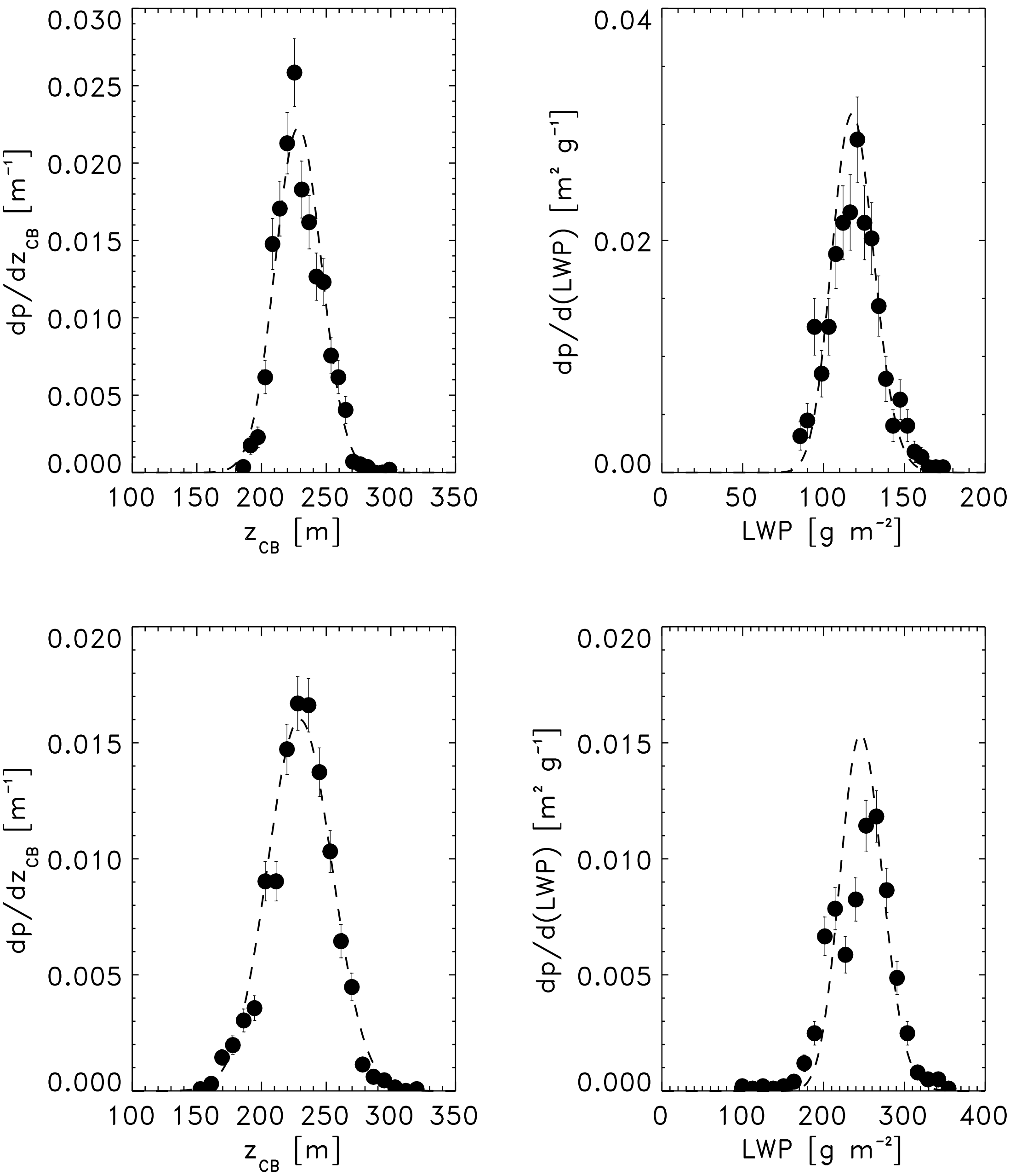

0.030
0.025
0.020
0.015
0.010
0.005
0.000
dp/dz$_{CB}$ [m^{-1}]
100 150 200 250 300 350
z$_{CB}$ [m]
0.04
0.02
0.00
dp/d(LWP) [m^2 g^{-1}]
0 50 100 150 200
LWP [g m^{-2}]
0.020
0.015
0.010
0.005
0.000
dp/dz$_{CB}$ [m^{-1}]
100 150 200 250 300 350
z$_{CB}$ [m]
0.020
0.015
0.010
0.005
0.000
dp/d(LWP) [m^2 g^{-1}]
0 100 200 300 400
LWP [g m^{-2}]

Figure 6:

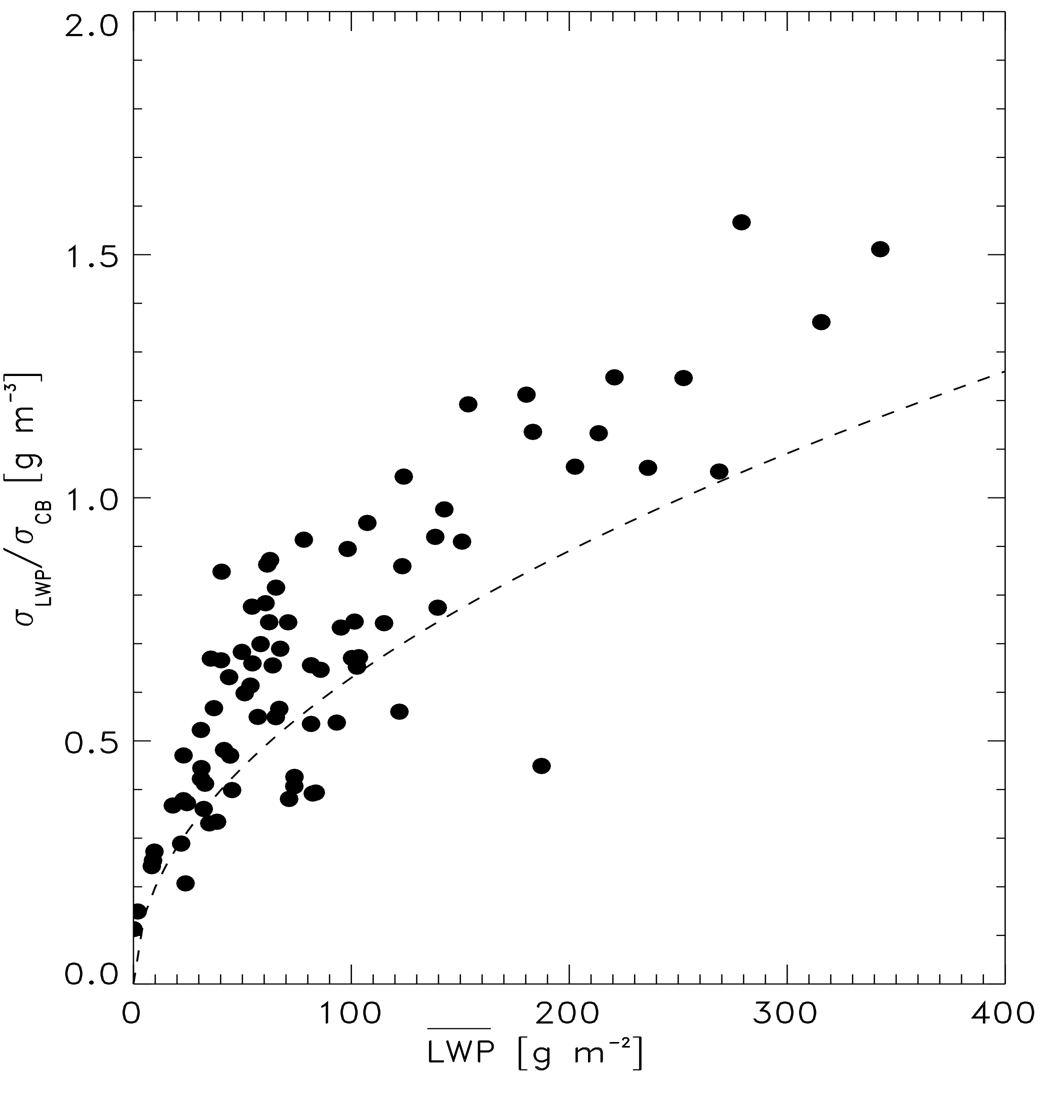

2.0
1.5
1.0
0.5
0.0
0
100
200
300
400
σ_{LWP}/σ_{CB} [g m^{-3}]
$\overline{LWP}$ [g m^{-2}]

Figure 7:

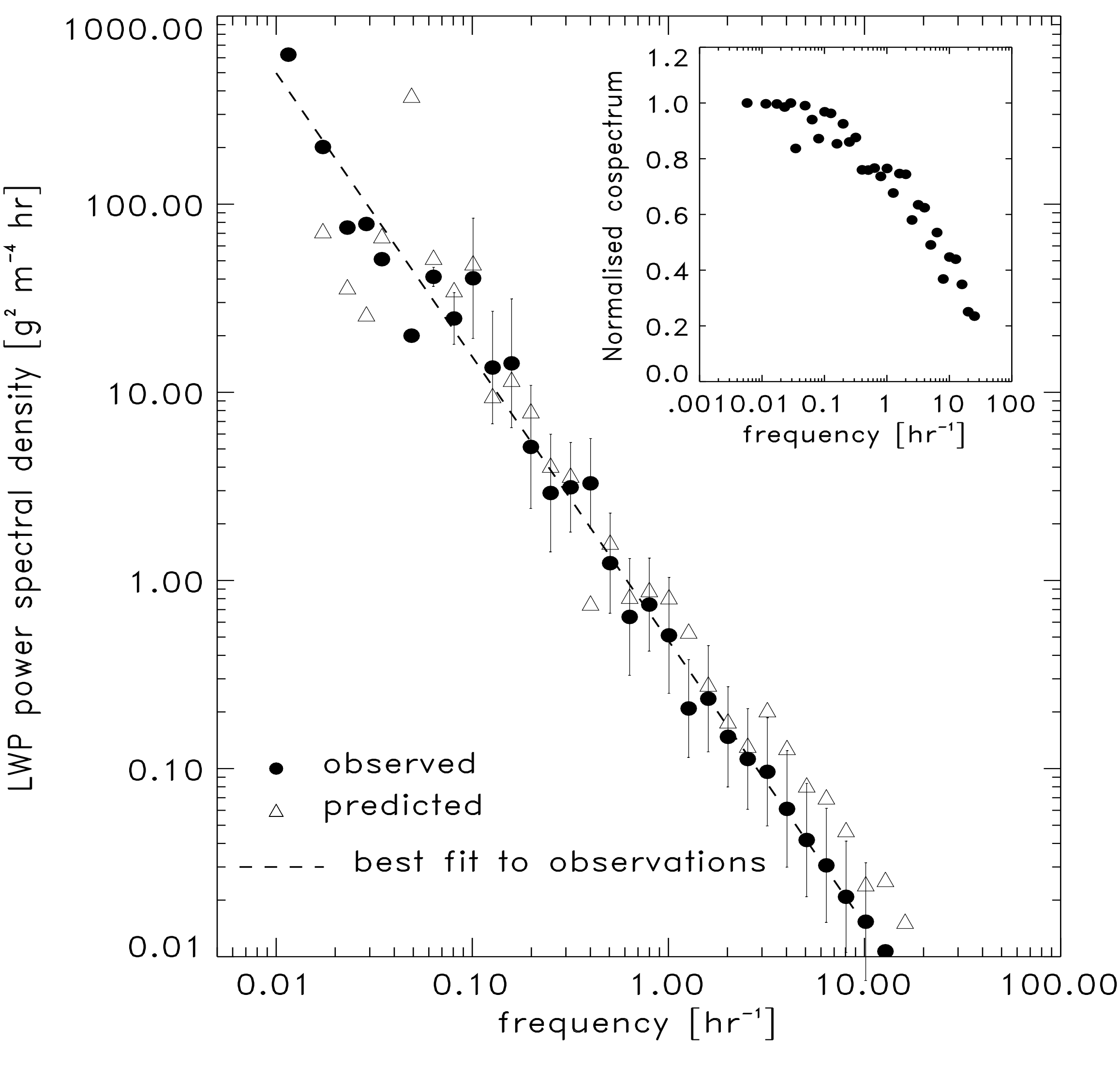

1000.00
100.00
10.00
1.00
0.10
0.01
0.01
0.10
1.00
10.00
100.00
LWP power spectral density [g² m⁻⁴ hr]
frequency [hr⁻¹]
observed
predicted
best fit to observations
1.2
1.0
0.8
0.6
0.4
0.2
0.0
Normalised cospectrum
.0010.01 0.1 1 10 100
frequency [hr⁻¹]

Figure 8:

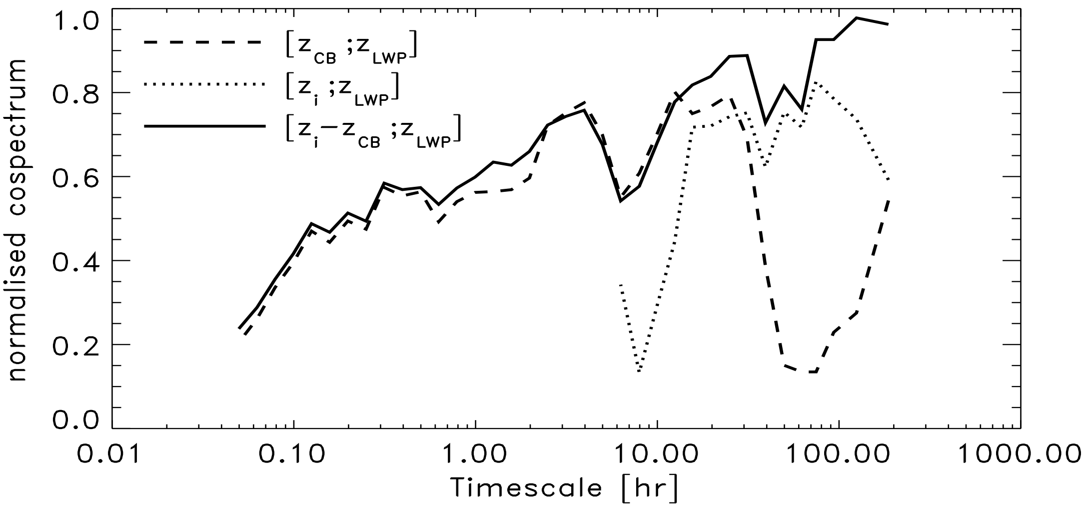

1.0
0.8
0.6
0.4
0.2
0.0
normalised cospectrum
0.01
0.10
1.00
10.00
100.00
1000.00
Timescale [hr]
[z_{CB} ;z_{LWP}]
[z_i ;z_{LWP}]
[z_i−z_{CB} ;z_{LWP}]

Figure 9:

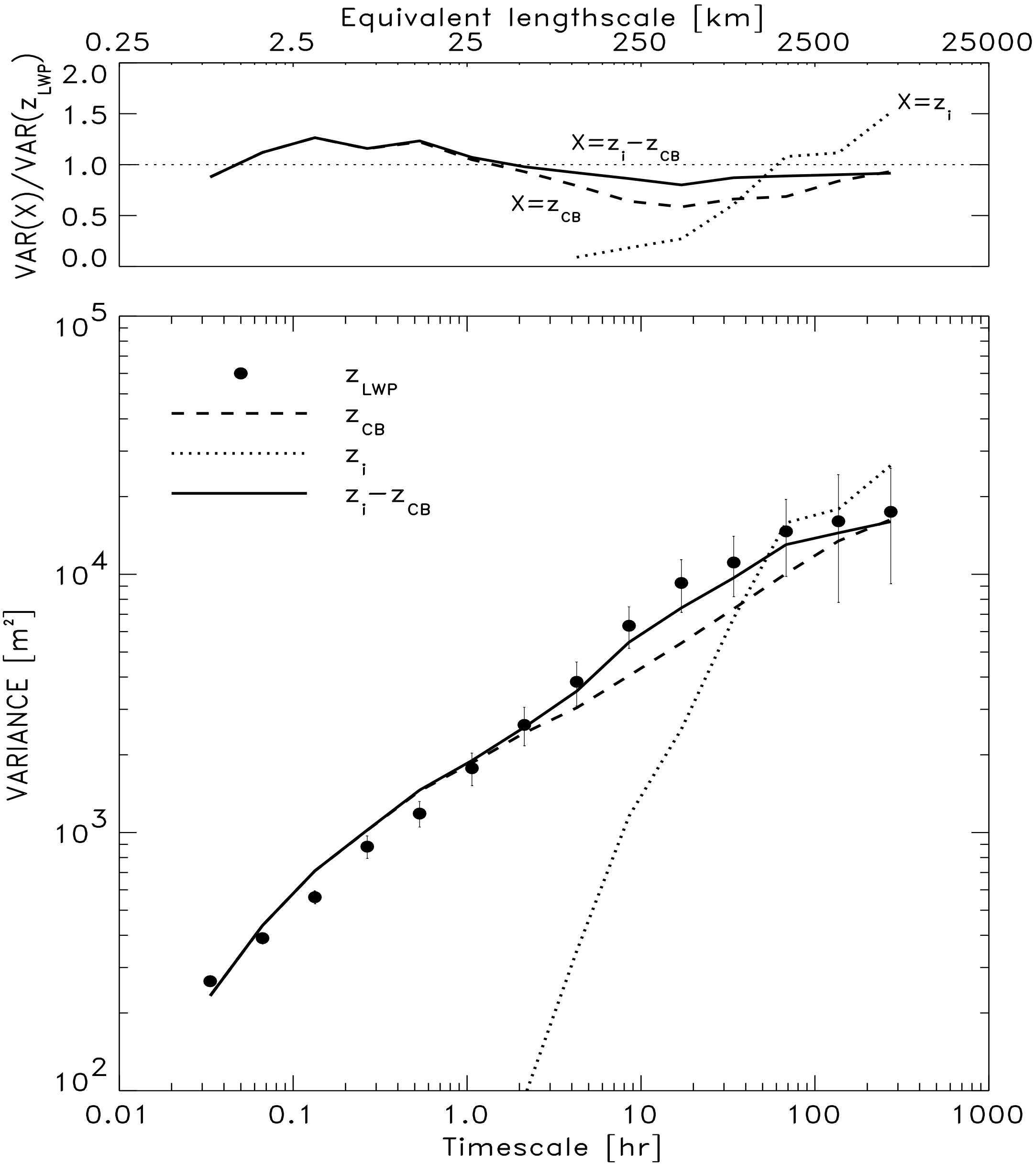
Equivalent lengthscale [km]
0.25
2.5
25
250
2500
25000
VAR(X)/VAR(z_LWP)
2.0
1.5
1.0
0.5
0.0
X=z_i
X=z_i−z_CB
X=z_CB
10^5
10^4
10^3
10^2
z_LWP
z_CB
z_i
z_i−z_CB
VARIANCE [m²]
0.01
0.1
1.0
10
100
1000
Timescale [hr]

Figure 10:

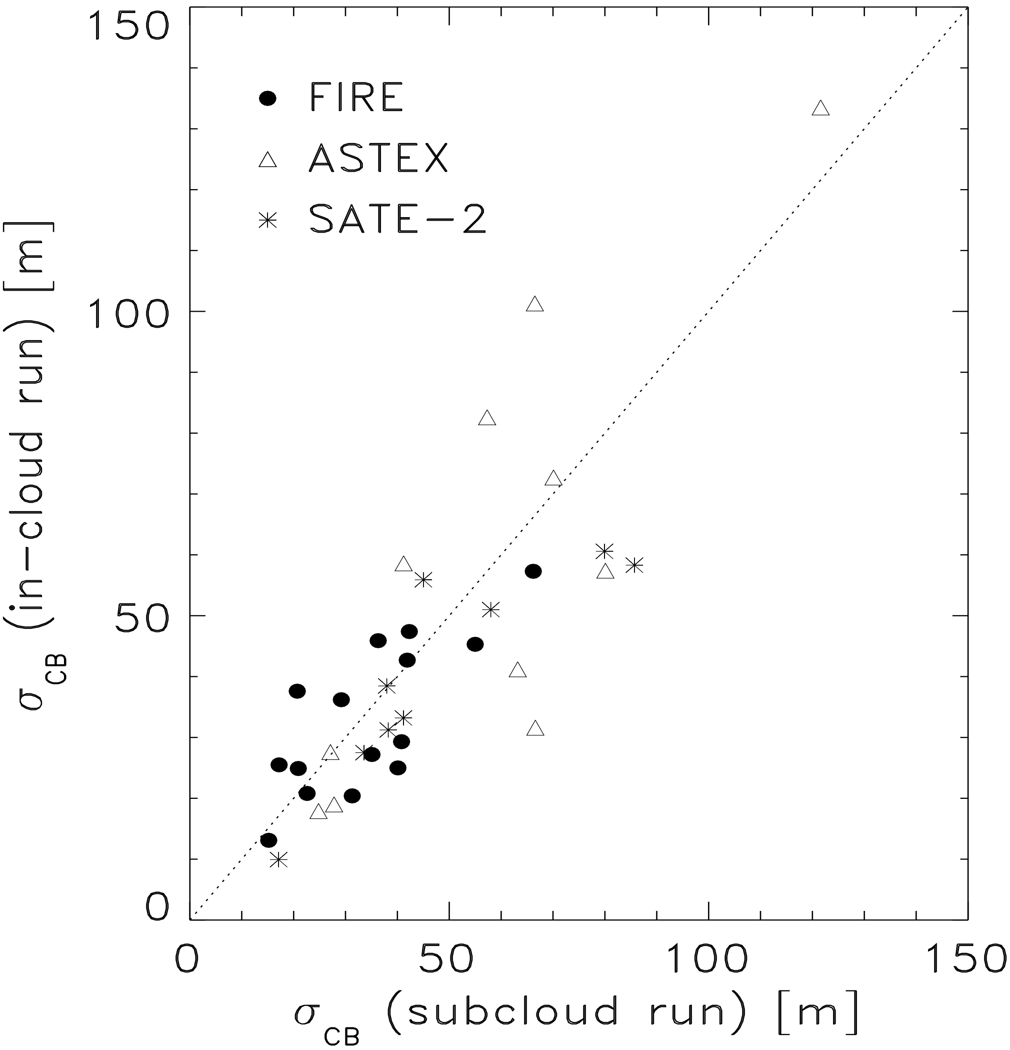
150
100
50
0
FIRE
ASTEX
SATE−2
σ_{CB} (in−cloud run) [m]
0
50
100
150
σ_{CB} (subcloud run) [m]

Figure 11:

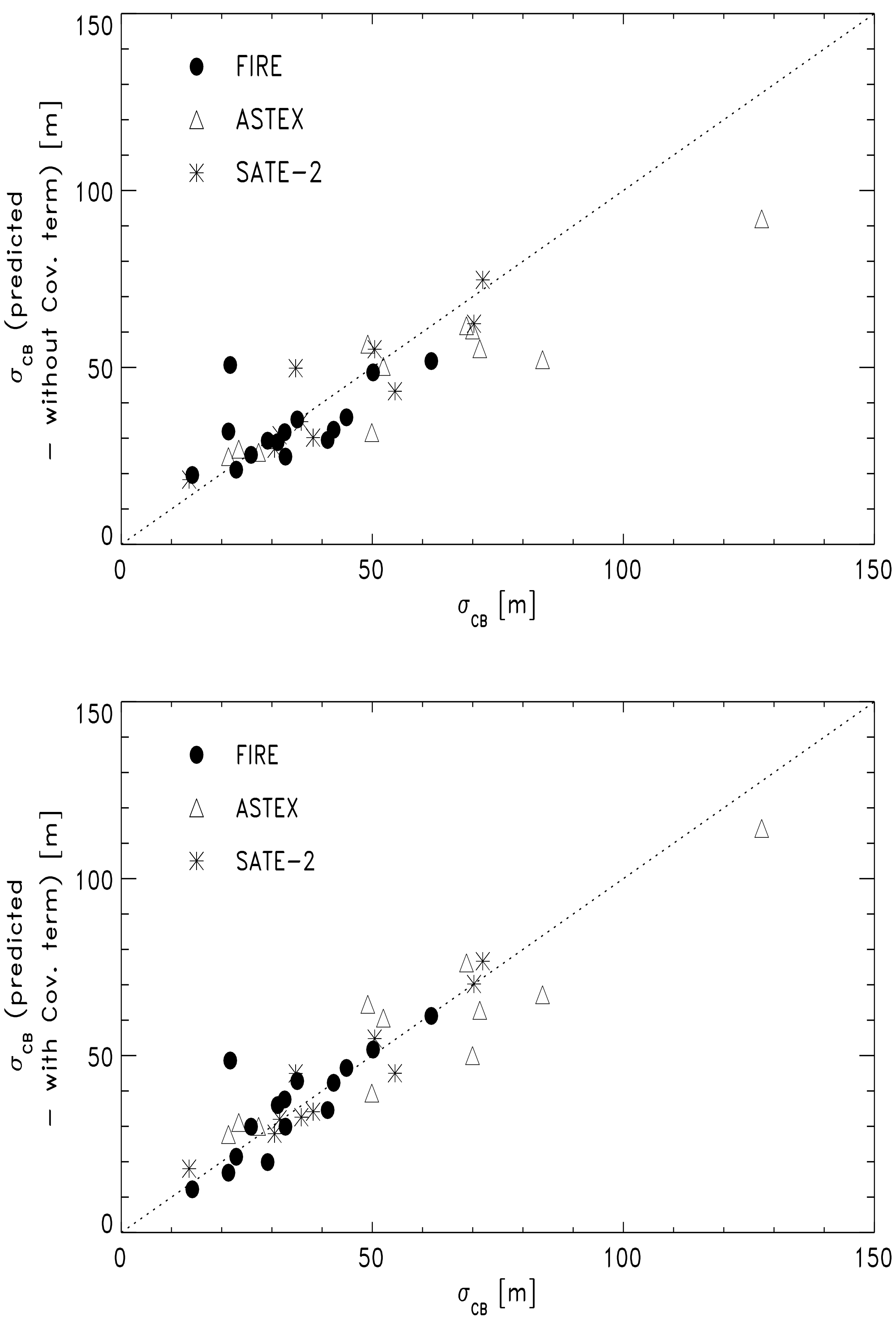
FIRE
ASTEX
SATE-2
σ_{CB} (predicted – without Cov. term) [m]
σ_{CB} [m]
FIRE
ASTEX
SATE-2
σ_{CB} (predicted – with Cov. term) [m]
σ_{CB} [m]

Figure 12:

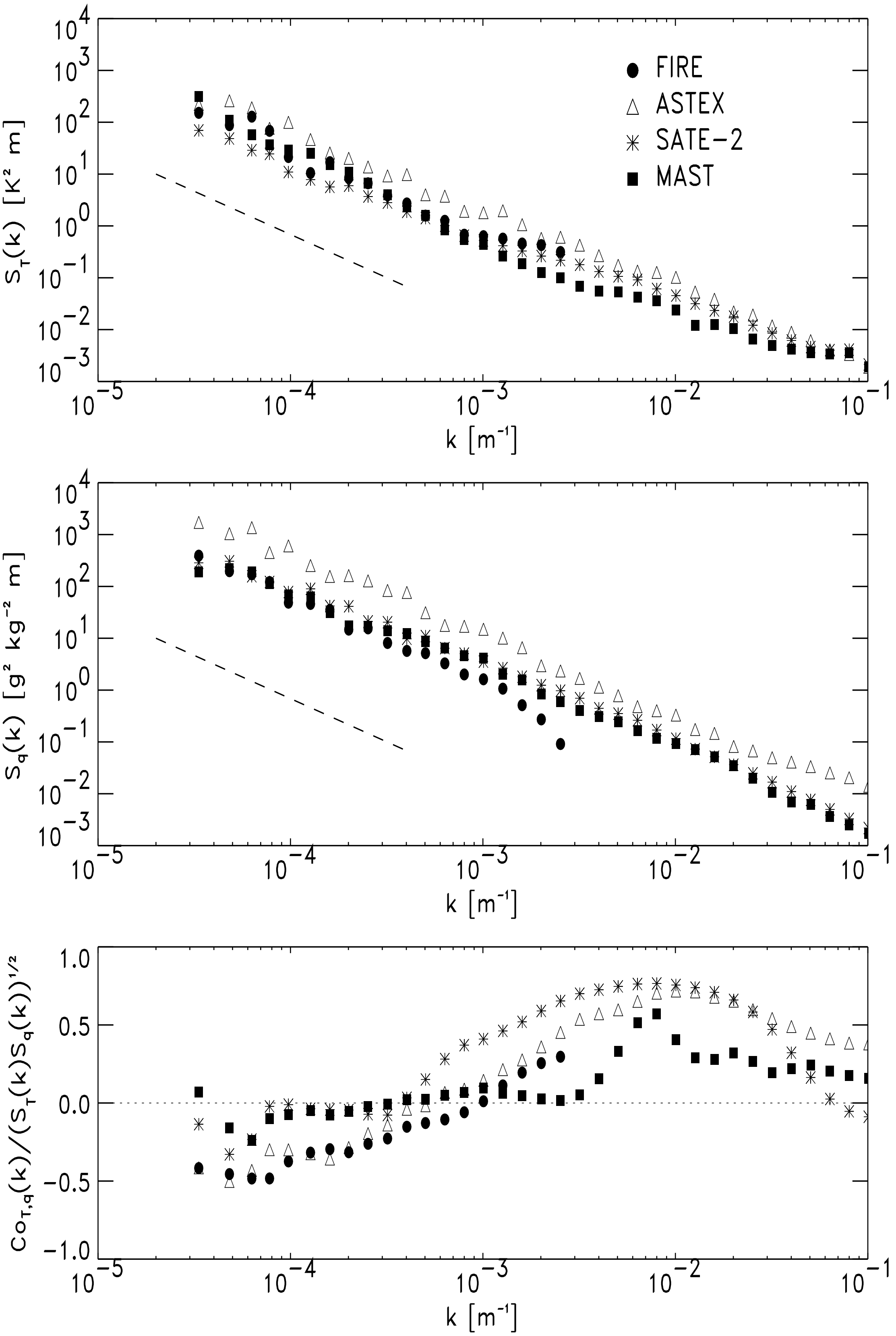

Figure 13:

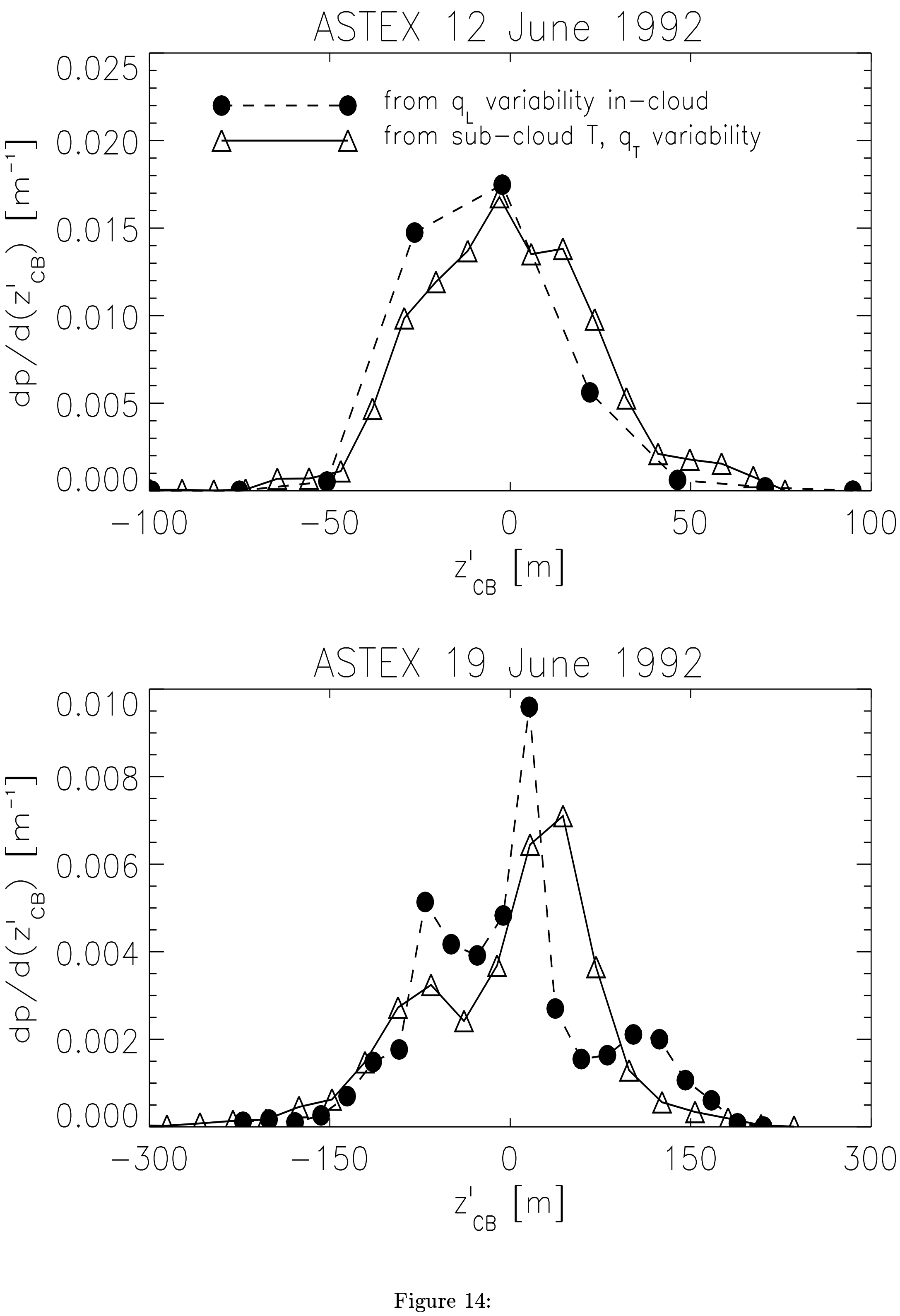
ASTEX 12 June 1992
from q_L variability in-cloud
from sub-cloud T, q_T variability
dp/d(z'$_{CB}$) [m^{-1}]
0.025
0.020
0.015
0.010
0.005
0.000
−100
−50
0
50
100
z'$_{CB}$ [m]
ASTEX 19 June 1992
dp/d(z'$_{CB}$) [m^{-1}]
0.010
0.008
0.006
0.004
0.002
0.000
−300
−150
0
150
300
z'$_{CB}$ [m]

Figure 14:

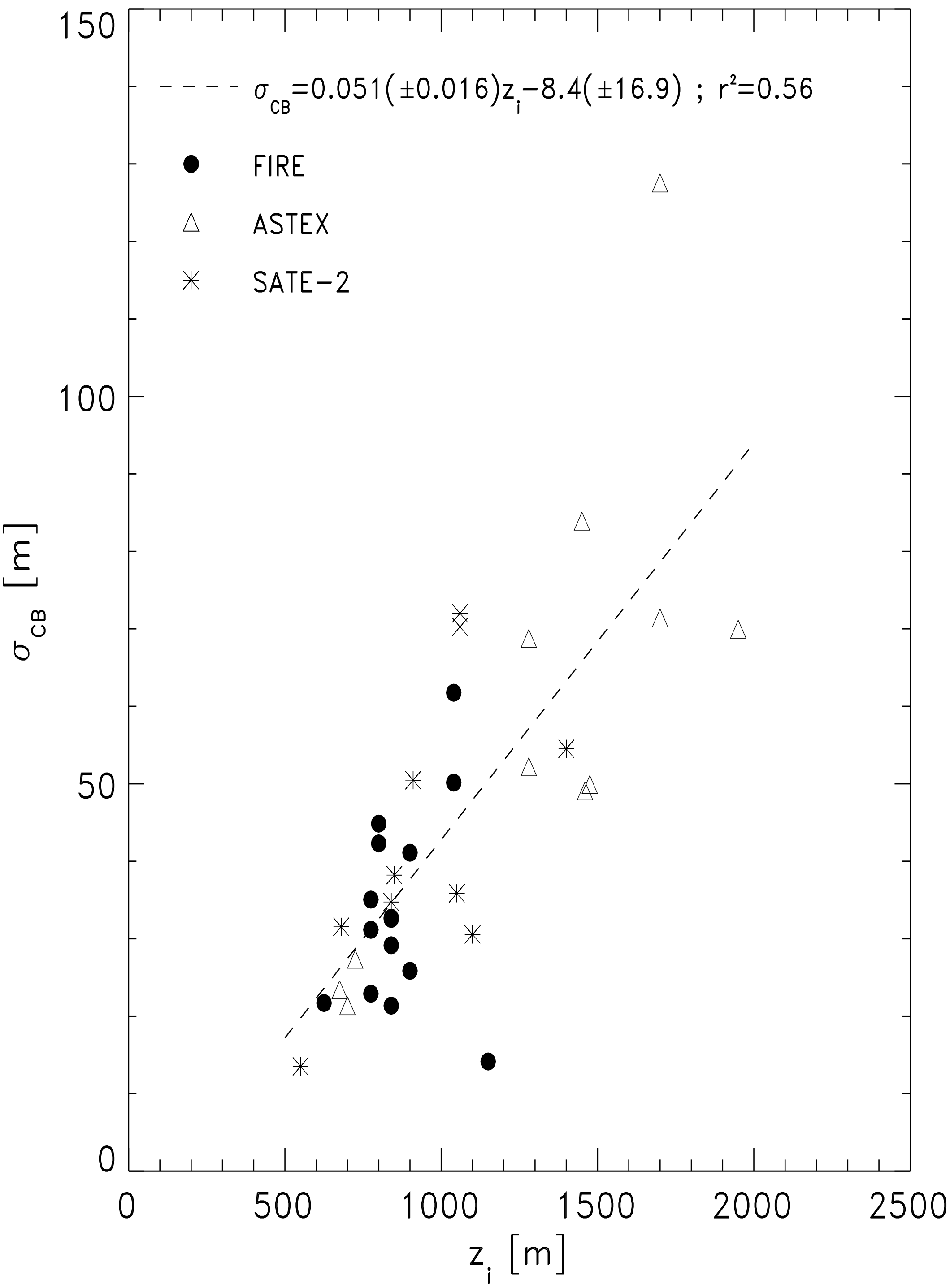

150
100
50
0
0
500
1000
1500
2000
2500
$\sigma_{CB}=0.051(\pm0.016)z_i-8.4(\pm16.9)$; $r^2=0.56$
FIRE
ASTEX
SATE-2
σ_{CB} [m]
z_i [m]

Figure 15:

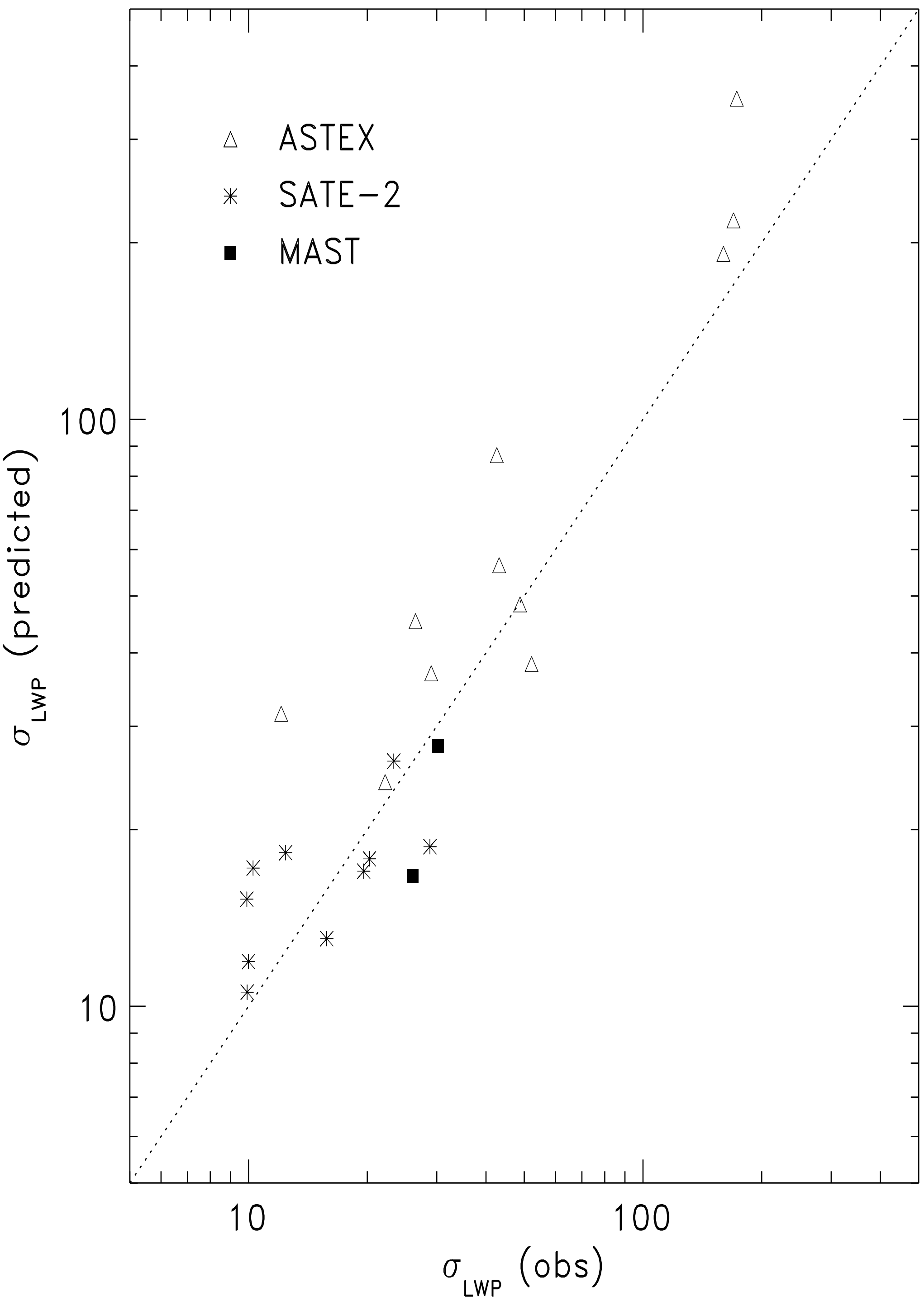
ASTEX
SATE-2
MAST
100
10
10
100
σ_{LWP} (predicted)
σ_{LWP} (obs)

Figure 16: